Temporal variations and trends of CFC11 and CFC12 surface-water saturations in Antarctic marginal seas: Results of a regional ocean circulation model

Christian B. Rodehacke [*]   Wolfgang Roether
Hartmut H. Hellmer   Timothy Hall

Version (Date March 6, 2009)

Abstract

The knowledge of chlorofluorocarbon (CFC11, CFC12) concentrations in ocean surface waters is a prerequisite for deriving formation rates of, and water mass ages in, deep and bottom waters on the basis of CFC data. In the Antarctic coastal region, surface-layer data are sparse in time and space, primarily due to the limited accessibility of the region. To help filling this gap, we carried out CFC simulations using a regional ocean general circulation model (OGCM) for the Southern Ocean, which includes the ocean-ice shelf interaction. The simulated surface layer saturations, i.e. the actual surface concentrations relative to solubility-equilibrium values, are verified against available observations. The CFC input fluxes driven by concentration gradients between atmosphere and ocean are controlled mainly by the sea ice cover, sea surface temperature, and salinity. However, no uniform explanation exists for the controlling mechanisms. Here, we present simulated long-term trends and seasonal variations of surface-layer saturation at Southern Ocean deep and bottom water formation sites and other key regions, and we discuss differences between these regions. The amplitudes of the seasonal saturation cycle vary from 22% to 66% and their long-term trends range from 0.1%/year to 0.9%/year. The seasonal saturation maximum lags the ice cover minimum by two months. We show that ignoring the trends and using instead the saturations actually observed can lead to systematic errors in deduced inventory-based formation rates by up to 10% and suggest an erroneous decline with time.

Key words: tracers, chlorofluorocarbons, gas flux, Antarctic Bottom Water, Southern Ocean, numerical model, formation rate, tracer inventory

[*] *Present address:* Christian B. Rodehacke, Zentrum für Marine and Atmosphären Wissenschaften, Institut für Meeresforschung, Hamburg, Germany; email: christian.rodehacke@zmaw.de

1

1 Introduction

Ocean tracer observations are a powerful tool to understand the formation and spreading of water masses. Sampling for the chlorofluorocarbons CFC11 and CFC12 has become a routine on many physical oceanography cruises, resulting in a large number of observations, in particular since the WOCE period (Orsi et al., 2002). Often, only tracer measurements highlight the spreading paths of freshly ventilated water masses, which stand out as spatially limited regions with tracer concentrations higher than in the surrounding waters.

Compared to the "classical" tracers, like oxygen and nutrients, anthropogenic CFC11 and CFC12 have the advantage to be chemically inert. CFCs enter the ocean by gas exchange across the ocean-atmosphere interface. Since their first appearance in the 1930s and up to around the turn of the millennium (Walker et al., 2000), the atmospheric concentrations increased (Fig. 13a), which is reflected in the temporal evolution of their concentrations in the ocean. This transient signal allows one to derive for tracer-carrying water masses

- tracer ages, for example, Weiss et al. (1985); Thiele and Sarmiento (1990); Doney et al. (1997),

- age/transit time distributions (TTD), for example, Beining and Roether (1996); Hall et al. (2002); Waugh et al. (2002, 2003),

- formation and subduction rates, for example, Broecker et al. (1999); Orsi et al. (1999); Meredith et al. (2001); Smethie and Fine (2001); Rhein et al. (2002).

Table 1 lists observed mixed layer saturations in high latitudes, where the CFC saturation is defined as the ratio of the actual concentration to the concentration in equilibrium with the atmospheric CFC partial pressure. For deeper waters, similarly, one uses the term "apparent saturation", the reference concentration being the concurrent equilibrium concentration at the ocean surface at the observed temperature and salinity. This saturation is termed apparent, since it ignores the fact that, when the waters actually descended from the mixed layer, the equilibrium concentration was lower than the concurrent one. Consequently, the apparent saturation is lower than the actual.

On the microscopic scale, CFC uptake occurs by diffusion through the oceanic skin layer on top of the mixed layer. The process is rather slow (equilibration time scale for a 100-m deep mixed layer is on the order of one month) so that the actual CFC uptake is controlled by mixed layer processes, essentially the exchange between the mixed layer and deeper layers (mixed layer entrainment/detrainment). The resulting undersaturation (Table 1) defines the air-water CFC gradient, to which the CFC uptake is proportional. Consequently, the sequestration of fluid in the seasonal thermocline and variations in the depth of mixing are primary factors (Haine and Richards, 1995), which need to be adequately represented for a realistic simulation of tracer concentrations and inventories in deep and bottom waters (Doney and Jenkins, 1988). Vertical mixing and other dynamical factors in the upper ocean are also essential for a realistic simulation of the Southern Ocean's hydrographic structure and sea ice coverage (Timmermann and Beckmann, 2004).

Region Year	Saturation [%]	Source	Abbr.
Shelf water mass at Antarctic's Periphery			
unspecified	40–60	Orsi et al. (2001)	
Ross Sea			
1984	CFC11: 64	Trumbore et al. (1991); and	
1984	CFC12: 79	Smethie and Jacobs (2005)	R:1
1994	CFC11: 74	Smethie and Jacobs (2005)	R:2
1994	CFC12: 79		
1994	60–70/90	Orsi et al. (2002)	R:3
2000	CFC11: 84	Smethie and Jacobs (2005)	R:4
2000	CFC12: 90		
2000/2001	72–95	Rivaro et al. (2004)	R:5
Wilkens Land			
1994	70	Orsi et al. (2002)	
Amery Ice Shelf, Prydz Bay			
1994	70	Orsi et al. (2002); Haine et al. (1998)	A:1
Central Weddell Sea			
1987	90	Mensch et al. (1996)	W:2
1992	65	Sültenfuß (1998)	
1996	85	Sültenfuß (1998)	W:3
Western Weddell Sea			
1992	55–85	Mensch et al. (2000)	W:1
1996	65	Sültenfuß (1998)	W:4
2004	68–70	Huhn et al. (2008)	W:5
Southern Weddell Sea, in front of the Filchner Ice Shelf			
1985	85	Mensch et al. (1996)	F:1
1987	65	Mensch et al. (1996)	F:2
1987	70-75	Schlosser et al. (1991)	F:3
1993	85–90	Gammelsrød et al. (1994)	F:4
Labrador Sea (Northern hemisphere)			
1986	60	Wallace and Lazier (1988)	
1988–1992	60–70	Smethie et al. (2000); and Smethie and Fine (2001)	
1988–1992	66	Terenzi et al. (2007)	
1997	CFC11: 90±8	Azetsu-Scott et al. (2005)	
1997	CFC12: 95±9		

Table 1: Observed CFC saturations in the ocean mixed layer. The abbreviations of the last column are for reference further below. Separately reported values for CFC11 and CFC12 are indicated.

In the Southern Ocean, the interaction with sea ice, the ice shelves, and the atmosphere transforms local water masses into deep and bottom waters. On broad continental shelves the accumulation of High Salinity Shelf Water (HSSW) due to brine release by sea ice formation initiates two known mixing processes, namely:

- The Foldvik- or ISW-process (Foldvik et al., 1985): HSSW flows into ice shelf caverns where it is modified to Ice Shelf Water (ISW) due to the interaction with the ice shelf base.

- The Foster-Carmack process (Foster and Carmack, 1976): Locally formed HSSW mixes with pycnocline waters penetrating onto the continental shelf.

Both mixing products descend along the continental slope under entrainment of ambient water masses to form deep or bottom water, depending on the entrainment rate.

During the transition from winter to summer, melting sea ice forms a seasonal halocline at 20–50 m depth (Carmack, 1974). The Antarctic Surface Water (ASW) above it has temperatures and salinities ranging from -1.8°C to 2.0°C and from 33.0 to 34.3, respectively. The deeper layer, called Winter Water (WW) (Carmack, 1974), maintains the characteristics of the Winter Mixed Layer (WML) with temperatures near the surface freezing point.

Since the beginning of CFC observations in the Southern Ocean marginal seas in 1985 (Mensch et al., 1996), observations, which have primarily been collected during the austral summer, remain sparse in space and time. Therefore, it has been common to assume a time-invariant saturation on the basis of the available data (Table 1).

Surface-water saturations can be converted into air-sea CFC fluxes using published parameterizations of gas exchange (Liss and Merlivat, 1986; Wanninkhof, 1992; Asher and Wanninkhof, 1998; Wu, 1996), and the effects have been studied in various numerical modeling efforts (England et al., 1994; Heinze et al., 1998). The most comprehensive comparison between simulated flux rates is found in Dutay et al. (2002) who compare the CFC distributions in thirteen global OGCMs. In the framework of the GOSAC (2002) project cumulative CFC fluxes were determined for the world ocean. A strong motivation is to apply the results to determine natural and/or anthropogenic carbon fluxes between the atmosphere and ocean (Terenzi et al., 2007; Takahashi et al., 2002).

Since existing CFC observations in surface waters are far from resolving the seasonal to interannual variability, we use a numerical regional ocean model (Section 2) to obtain more detailed information concerning the oceanic CFC uptake. The CFC input function can be expressed as a product of the unknown surface saturation together with the well-known atmospheric concentration history and solubility (Warner and Weiss, 1985). The model validation follows in section 3, which includes a detailed description of the available observed surface-water CFC saturations (Section 3.2) and the simulated CFC surface saturation distribution (Section 3.3). The strength of seasonal saturation cycles and long-term trends in the presence of sea ice are addressed in Section 4. We analyze the processes that drive the CFC fluxes across the atmosphere-ocean interface and present correlations and multi-linear regression analyses between a variety of parameters and the CFC fluxes to confirm our findings (Section 5.1). The discussion includes the effects of a time-dependent versus an invariant saturation on bottom/deep

4

water formation rates based on CFC inventories (Section 5.2), and the paper ends with concluding remarks (Section 6).

2 The model

Our model is the regional ocean circulation model BRIOS-1.0, a version of the s-coordinate primitive equation model SPEM (Haidvogel et al., 1991), adapted to the Southern Ocean by adding the major ice shelf cavities and their interaction with the ocean (Beckmann et al., 1999). The domain comprises the circumpolar ocean between $50°$S and $82°$S, has a resolution of $1.5° \times 1.5° \cos\phi$ in the Atlantic Sector, which increases gradually to $6.75° \times 1.5° \cos\phi$ outside the Atlantic, and has 24 terrain-following vertical coordinates to better represent both mixed layer and near-bottom processes. The model is forced by fluxes obtained from a standalone sea ice-mixed layer model for the same area using a climatological year based on ECMWF data of the period 1985–1997. The model is integrated for 20 model-years to reach a quasi-stationary dynamical state, thereafter the CFC simulation starts with year 1940.

According to Beckmann et al. (1999), who present details of the model setup, the lateral diffusivity ($\nu_{T,S}$) depends linearly on the grid size (Δ) and local flow field. It resembles an upstream scheme acting along geopotential surfaces. At the surface and the bottom a background diffusivity of $\nu_{T,S}^{\mathrm{back}} = \Delta 2{\cdot}10^{-2}\,\mathrm{ms}^{-1}$ was added to represent enhanced levels of turbulence in the boundary layers and wind-induced, near-surface mixing.

The parameterization of the vertical mixing in the Southern Ocean is critical for a realistic representation of the observed hydrographic structure (Timmermann and Losch, 2005; Timmermann and Beckmann, 2004; Beckmann et al., 1999) and certainly influences the uptake of tracers, as shown by Doney and Jenkins (1988) and Haine and Richards (1995). The vertical viscosity and diffusivity are computed as Richardson-number-dependent functions according to Pacanowski and Philander (1981). An explicit scheme was employed for vertical diffusivity, which is the most critical value as sensitivity studies of initial parameters revealed. The weak stratification in the salinity-dominated regime reacts very sensitively to large vertical diffusivities, which unrealistically homogenize rapidly the Weddell Sea down to 2000 m depth. Therefore, the maximum diffusivity is $\kappa = 0.01\,\mathrm{m}^2 s^{-1}$ in case of small or negative Richardson numbers. Under the assumption of a continuous forcing, this maximum vertical diffusivity is analog to convective processes, which homogenize within a day a water column of 30 m thickness. This is a reasonable assumption for a grid size of hundreds to thousands kilometers.

The used sea ice concentration climatology (A) agrees on the large scale reasonable well with satellite and ULS data (Timmermann, 2000); details of the coupled sea ice-ocean model version are described by Timmermann et al. (2002).

The tracer input is implemented as a flux boundary condition according to Asher and Wanninkhof (1998). It is controlled by the concentration gradient across the air-sea interface, with the wind velocity modulating the flux rate (Wanninkhof, 1992). Since sea ice prevents gas exchange, the flux is reduced by the grid box fraction covered with

5

159 ice (A) according to England et al. (1994). The gas exchange is obtained as

$$F_G = k_0 \underbrace{(\overbrace{\alpha_s p_{\mathrm{atm}}}^{c_{100\%}} - c_{\mathrm{w}})}_{=\Delta c} (1 - A) \frac{u_{10}^2}{\sqrt{\mathrm{Sc}}}, \tag{1}$$

where k_0 is the piston velocity — derived from bomb-produced radiocarbon invasion rates into the ocean and, hence, includes implicitly the Schmidt number for $^{14}\mathrm{C}$ —
162 (England et al., 1994), p_{atm} the temporal evolution of the atmospheric concentration (Walker et al., 2000), α_s the solubility (Warner and Weiss, 1985), $c_{100\%}$ the equilibrium concentration, c_{w} the surface concentration, and Sc the Schmidt number (Zheng
165 et al., 1998). The wind influence is considered by using a computed spatial seasonal cycle of squared winds (u_{10}^2), which represents a climatological mean state. In the northern relaxation zone, the subsurface CFC concentrations are nudged towards zero,
168 considering that the water masses that flow towards the deep and bottom water formation sites have negligible CFC concentrations (Roether et al., 1993). Further details about chlorofluorocarbon boundary conditions and CFC simulation results are found
171 in Rodehacke et al. (2007).

The saturation in each grid box is obtained as the ratio of the modeled concentration driven by the flux boundary condition (Eq. 1) and the model result in which the ocean
174 surface concentration is held at a solubility equilibrium, i.e.,

$$c_{\mathrm{w}}(t) = \alpha_s(\Theta(t), S(t)) \ p_{\mathrm{atm}}(t) = c_{100\%}(t). \tag{2}$$

This boundary condition implies a nearly infinite gas flux when a surface grid box is under- or oversaturated. To ensure identical conditions for all tracers regardless of their
177 boundary condition, we performed all tracer simulations simultaneously.

3   Model Validation

The validation of the dynamical model setup is described by Beckmann et al. (1999)
180 a nd is partly recapitulated here. The flow field reproduces the known circulation features: the eastward flowing Antarctic Circumpolar Current (ACC), the cyclonic Weddell, Ross and Kerguelen Gyres as well as the Antarctic Coastal Current, where ob-
183 served rates agree with the simulated transports of both Weddell Gyre cells. Simulated annual mean fields of temperature and salinity (Figs. 9a and 9b in Beckmann et al. (1999))along the Joinville Island-Cap Norvegia section reproduce well the observed
186 doming (Figs. 7a and 7b in Fahrbach et al. (1994)).

A unique feature of this model is the integration of major ice shelf caverns including the ocean-shelf ice interaction. Each cavern has its own signature in the Θ-S-space
189 (Rodehacke et al. (2007), Fig. 4). Furthermore, the caverns are a source of relatively cold and fresh water masses, which change, in particular, the properties of the near-surface layers. These are distinctly fresher (up to -0.22) and cooler (up to -1.5°C)
192 (Figures 13a and 13b in Beckmann et al. (1999)). Since the upper water column of the western Weddell Sea is stabilized by these lighter water masses, convection is reduced which preserves the warmer and saltier deep water masses.

6

As the Θ-S-diagram shows, the model reproduces the linear mixing between ISW and WSDW. On the continental shelf in front of Filchner-Ronne Ice Shelf (FRIS) observed and simulated hydrographic properties and helium saturations, which are strongly determined by the addition of glacial melt due to ocean–ice shelf interaction, indicate that the model reproduces the general hydrographicstructure and the ISW outflow. Furthermore, the analysis highlights the importance of the ocean-ice shelf interaction but also suggests that model resolution might be too coarse to prevent warm and salty water masses from penetrating onto the continental shelf (Rodehacke et al., 2006). Nevertheless, a comprehensive treatment of the sub-ice shelf environment and the related freshwater fluxes seems to be important for an adequate representation of observed local and large-scale hydrographic conditions (Hellmer, 2004).

For the model setup used here, the spread of CFC-carrying water masses indicates the paths of freshly formed deep and bottom water (Rodehacke et al., 2007). In agreement with observations (e.g. Baines and Condie (1998)), the model reproduces the main deep and bottom water formation sites in, e.g., the Ross Sea and the southwestern Weddell Sea (Rodehacke et al. (2007), Fig. 8). These areas are located on the continental shelves with depths commonly shallower than 500 m. The upper 100 m of the water column are thus represented by nine (seven) layers for a depth of 500 m (1000 m).

Along two sections following the Greenwich Meridian (Rodehacke et al. (2007), Fig. 10) and the WOCE SR4 section from Joinville Island to Cap Norvegia (Rodehacke et al. (2007), Fig. 9), the vertical simulated CFC distributions show a well ventilated upper mixed layer, which is separated from lower water masses by a sharp concentration gradient. The simulated gradient seems to be stronger than the CFC observations suggest. Along the coast wind induced downward Ekman pumping deepens the mixed layer, which is in accordance with observations. In addition, CFC-inventories along the Greenwich Meridian (Rodehacke et al. (2007), section 6.1), which are dominated by mixed layer concentrations, agree reasonably well with observations from the years 1992, 1996, and 1998 (Rodehacke et al. (2007), Section 6.1). However, the simulated CFC distribution has deficiencies, i.e, the ventilation of water masses below $\approx$1580 m is underestimated. The model does not reproduce subsurface cores clearly separated from the surface mixed layer, and the cores are in general too wide, probably caused by an insufficient horizontal model resolution (Rodehacke et al., 2007), but the latter agrees with the results from models of similar resolution (e.g. Fichefet and Goosse (1999); Doney and Hecht (2001); Dutay et al. (2002)).

Profiles of CFC concentrations at several locations north of the Weddell Gyre (Rodehacke et al. (2007), Fig. 13) show that the vertical structure agrees reasonable well with observations. However, the observed CFC concentration at profile 7 in the center of Drake Passage penetrates unusually deep $\sim$750 m, which seems to be associated with the Polar Front (Roether et al., 1993). Since the model does not resolve the frontal system, the model cannot reproduced this feature (Rodehacke et al. (2007)).

3.1 Mixed layer depth along the Greenwich Meridian

Since the temporal evolution of the mixed layer depth (MLD) influences the CFC uptake (Tab. 6), we validate simulated MLDs against observed ones. The comparison is restricted to the repeatedly sampled Greenwich Meridian, which allows us to infer the

7

deduced MLD uncertainty. Beginning at the surface, a density increase by 1% defines the pycnocline, which is the base of the mixed layer.

The observed MLD (Fig. 1) generally amounts to 50–200 m and reaches the sea floor south of Maud Rise (65°S). A MLD equal to the bottom depth does not necessarily imply a homogenized water column. Since both cruises, *ANT XIII/3* and *ANT XV/4*, occupied the Greenwich Meridian in May/June, their differences might be related to natural variability. In addition, neighboring observations also show distinct depth variability, like during *ANT XIII/3*, in the range of 75–140 m at 59°S or during *ANT XV/4* ranging from 600 m to 4800 m at 67°S. The latter might be attributed to the local conditions above Maud Rise, which will be discussed in section 5.1 (Fig. 18).
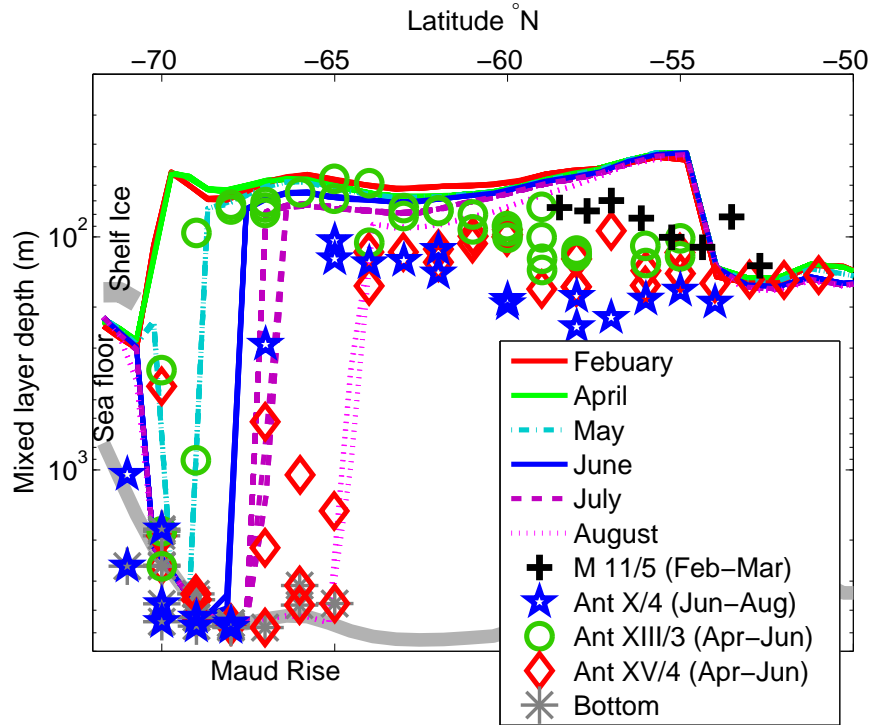
Figure 1: Observed and simulated mixed layer depth along the Greenwich Meridian (logarithmic ordinate). Symbols represent deduced values from observed bottle data for the listed cruises (see also Table 2), while simulated values for different months are represented by lines for a sequence of several years. If the observed mixed layer depth equals the depth of the deepest observation, its symbol is combined with a gray star. For clarity, observations are grouped in bands of 1°. The model topography is added as grey thick line and the model layers south of 71°S are located underneath the Ekström Ice Shelf. The seamount Maud Rise is marked.

The simulated MLD (Fig. 1) ranges from 45 m to 180 m, which is beneath the upper two model layers of enhanced background diffusivity ($\nu_{T,S}^{\text{back}}$, Section 2). The sequence

8

of the MLD against latitude from February to August reveals that the depths are nearly temporally invariant from February to April when sea ice is absent or melting. With the beginning of winter sea ice formation releases salt into the surface layer, which decreases the density gradient between surface and deeper layers and thus increases the MLD. Since the stratification is weak, the mixed layer can reach the bottom at the southern edge of the section.

The simulation agrees with the observed mixed layer depths north of $54°$S and south of $60°$S. Although in the south the model tends to underestimate the MLD, the natural variability along the complete section is larger than the mismatch. The simulated MLD local minimum around $55°$S, while the observed MLDs decrease towards north, is only manifested in the logarithmic depiction. The observed (*ANT X/4*, *ANT XIII/3*, and *ANT XV/4*) and simulated surface temperatures and surface salinities coincide along the Greenwich Meridian, except for salinity between $54°$S–$60°$S. Here, the simulated surface salinities decrease smoothly towards north while the observed salinities stay nearly constant up to $56°$S where they decrease abruptly by 0.1–0.15 (*ANT XIII/3*, *ANT XV/4*). This is probably related to the front which separates the so-called "cold regime" and "warm regime" (Gordon and Huber, 1984; Schröder and Fahrbach, 1999).

The difference between observed and simulated surface salinity is strongly related to the coarse model resolution, which does not resolve frontal systems. If we would replace the simulated surface salinities with observations, the MLD difference between $54°$S and $60°$S would vanish completely, emphasizing the in general reasonable representation of the subsurface density stratification in our model. The impact of the mixed layer difference on the CFC saturation along the Greenwich Meridian is discussed below (cf. Fig. 6).

3.2 Comparison of modeled and observed surface-layer saturations

Validating the modeled CFC surface-water saturations against observations is a crucial step in our analysis. One has to consider that the model is driven by a recurring annual cycle, so that the forcing does not include the observed extremes of, for example, sea ice concentration or wind speed. Furthermore, since we also compare observations at a single point with simulated, averaged values of a model grid box, we cannot expect to obtain a perfect match. In fact, the modeled CFC11 saturations (Fig. 2) appear systematically high for the observed lower saturations and fall short of the supersaturations of up to 110% (cruise *M11/5*). To assess this situation, we address the distribution of the model-data discrepancies in the model's Weddell Sea sector. We deduce an objective criterion for the inherent or natural CFC saturation spread in the upper surface layer, based on the maximum differences among the observed CFC11 saturations at each profile down to 55 m (Fig. 3). Under the most valid assumption that the upper 55 m of the water column are well mixed, the CFC variability of observed CFC saturations in the upper 55 m represents the natural spread of saturations. We interpret this quantity as natural uncertainty and call it "spread", which represents the "error bar" of the observed saturation within a homogenized water column during a cast. This variability or spread is much larger than the accuracy of measurement and represents the allowed/acceptable mismatch between single observation and simulation. For clar-
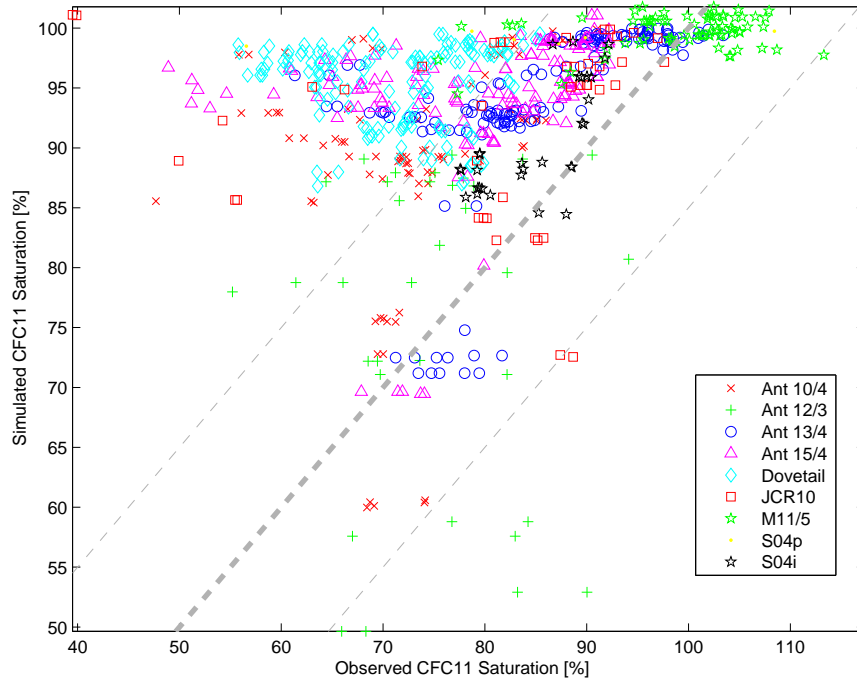
9

Figure 2: Simulated versus observed CFC11 saturations in the mixed layer for the period 1990–1998. The gray thick line represents the 1:1 relation while he thin dashed lines consider a difference of 15%. (For cruise details see Table 2).

ity, we also check the differences in sea ice concentration between observations and simulation.

3.2.1 CFC11 saturation spread ranges and model-data biases

For the model's Weddell Sea sector, the spatial distribution of CFC11 saturation differences between observations and simulation are shown in Figure 3 (upper left). If the absolute saturation difference is below 5%, the station is marked by a green star ('*'). Departures of more than 5% are tagged by either a circle (observed saturations are higher than the simulated one) or squares (observations are lower than the simulation), where the symbol size is proportional to the difference (see legend). If more than one observation exists at any position, all differences between these observations and the simulated values are displayed. The sea ice concentration differences (Fig. 3, lower left) show a somewhat similar distribution, although discrepancies near the southern margin tend to be higher. Shown are the differences one month prior to the observations, considering that the air-sea equilibration takes several weeks and the maximum simulated saturation occurs two months after the sea ice concentration minimum (Sec. 4.1). The grid size of the observed sea ice concentration data is 25×25 km. The accuracy of total sea ice concentration (δA) is approximately 5% (Cavalieri et al., 2005),

10
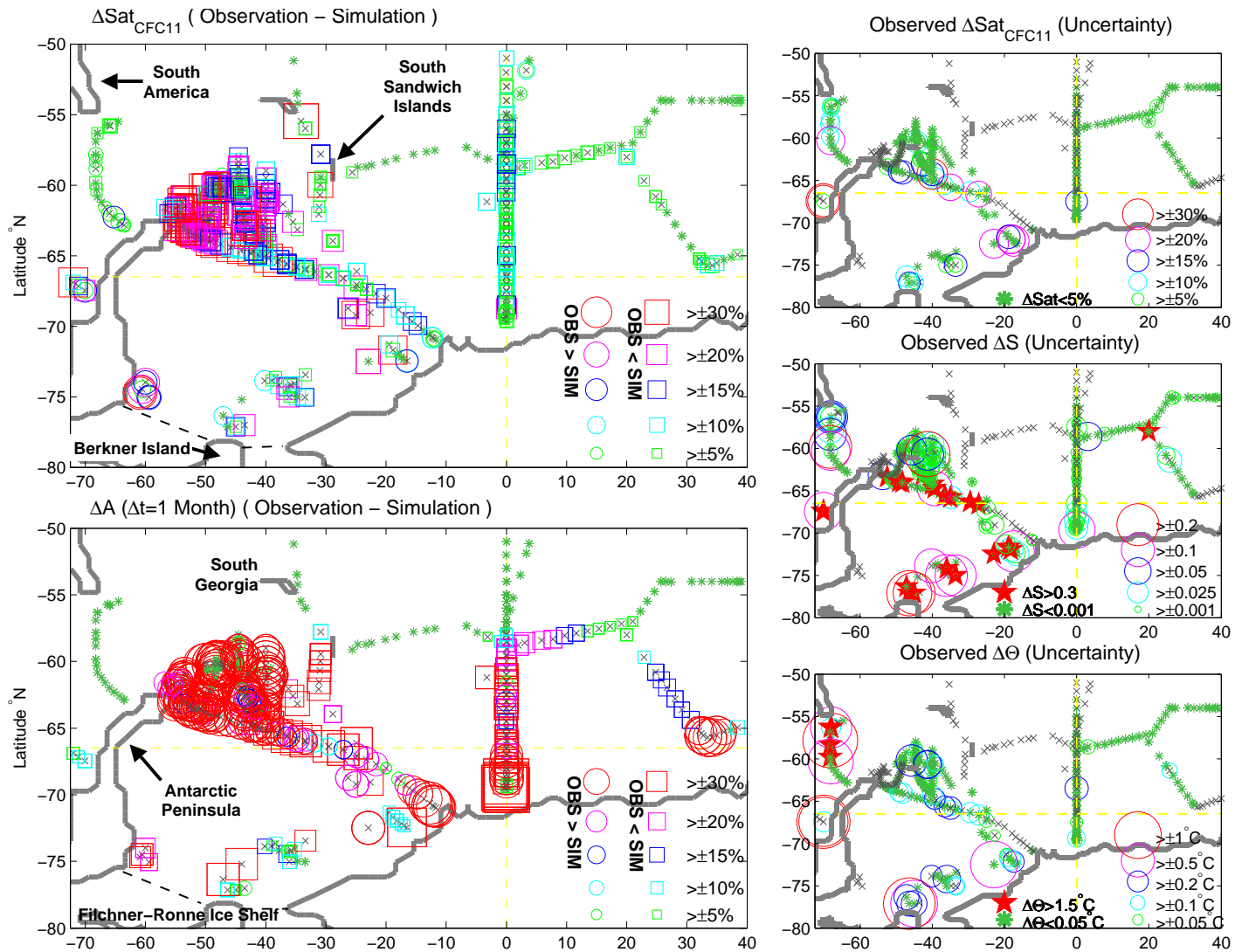
Figure 3: Spatial distributions of observed minus simulated values for the period 1990–1998 (left side). CFC11 saturation difference (ΔSat_{CFC11}, upper left), and sea ice concentration difference one month before the tracer measurements ($\Delta A(\Delta t)$) were taken (lower left). The observed sea ice concentrations are based on the Scanning Multichannel Microwave Radiometer (SMMR) and Special Sensor Microwave/Imager(SSM/I) data using the NASA Team algorithm. For the considered period the data set is derived from DMSP-F8, DMSP-F11, DMSP-F13 Special Sensor Microwave/Imager (SSM/I) daily brightness temperatures at every grid cell (Cavalieri et al., 2005). Difference of observed values, termed spread range, within the upper 55 m from all observations at each cast (right side). The upper, middle, and lower right figures show the spread of the CFC11 saturation (ΔSat_{CFC11}), salinity (ΔS), and temperature ($\Delta\Theta$), respectively. The location of each cast is indicated by an 'x'. Green stars ('*') denote differences or spreads below 5% (ΔSat_{CFC11}, ΔA) and spreads of temperature ($\Delta\Theta < 0.05°C$) and salinity ($\Delta S < 0.001$). Bold red stars ('⋆') depict extreme temperature and salinity spreads. Further details are provided by the corresponding legends (lower right of each figure).

but might be lower when melt ponds exist, in view of approximately 15% accuracy in the Arctic during summer (Cavalieri et al., 2005).

In order to characterize the spread of the observed data, we present for each station the maximum difference among the observed saturations within the upper 55 m (Fig. 3, upper right). If only one observation is available at a station, the spread is unknown and the corresponding station is marked by an 'x'. For stations of more than two observations, all combinations of differences between pairs of observations are shown, where the symbol size is proportional to the variability as indicated by the legend. For comparison, also the corresponding spread ranges of salinity and temperature (Fig. 3, middle and lower right) are presented, where we restrict our comparison to those depths where temperature, salinity, and CFC data are simultaneously collected.

Along the Greenwich Meridian, the simulated CFC11 saturations deviate by up to +20% absolute (observed saturation minus simulated saturation ($s_{obs} - s_{sim}$); Fig. 3, upper left, Fig. 6) from the corresponding observed values for all cruises (*ANT X/4*, *ANT XIII/4*, *ANT XV/4*, and *M11/5*, Tab. 2) which took place between February and June. The extreme mismatches between -48% and +16% absolute (observation minus simulation) are predominantly located at the dynamically active edge of the Weddell Gyre (coastal current, polar front, and sea ice edge). The maximal CFC11 spread is, in general, less than 5% absolute and reaches 18% absolute only within the coastal current (Fig. 3, upper right side). East of the Greenwich Meridian (*ANT XIII/4*, *M11/5*, and *SO4i*), the differences are mostly lower than +10% absolute and do not exceed +20% absolute, while the spread reaches values of up to 6% absolute. In the sea-ice free Drake Passage (*M11/5*) the saturation differences are between -22% and +16% absolute with a spread below 12% absolute, whereby large differences and high spread do not always coincide. In the southern Weddell Sea (*ANT XII/3*), the spread is below 16% while the differences are between -23% and +37% absolute. Here, shallower observations tend to show a better agreement with the simulation. A vast region of large discrepancies and high spreads is clustered east of the tip of the Antarctic Peninsula (Fig. 3, 57°S to 66°S, 32°W to 60°W). The saturation differences range from -48% to +16% absolute whereas the spread reaches values of up to 30% absolute. Evidently, the model-data differences consistently exceed the data spreads according to our criterion.

In the upper 55 m, the CFC saturation spread is, in general, 10%–20% absolute (Tab. 2). A higher spread often occurs in profiles for which the observed temperature and salinity spread is also high (Fig. 3, right side). This indicates that the assumption of a homogeneous CFC concentration in the upper 55 m might be invalid at some locations because of distinct vertical temperature and salinity gradients (Fig. 3). The gradients might be caused by melting sea ice, which freshens the upper water column and splits the winter mixed layer (WML) into Antarctic Surface Water (ASW) and WW (Carmack, 1974). Since WW has no contact with the atmosphere, a distinct CFC undersaturation developed during the preceding winter is preserved. In contrast, disequilibrium within the ASW is reduced by gas exchange across the ocean-atmosphere interface and by solar heating, which reduces the equilibrium concentration. Therefore, shallower samples have a higher saturation than the deeper ones. However, not all profiles with a high CFC saturation spread are related to an enhanced spread in temperature and/or salinity nor does a high temperature and/or salinity spread cause an increased saturation spread. Thus, a clear relationship between CFC saturation and
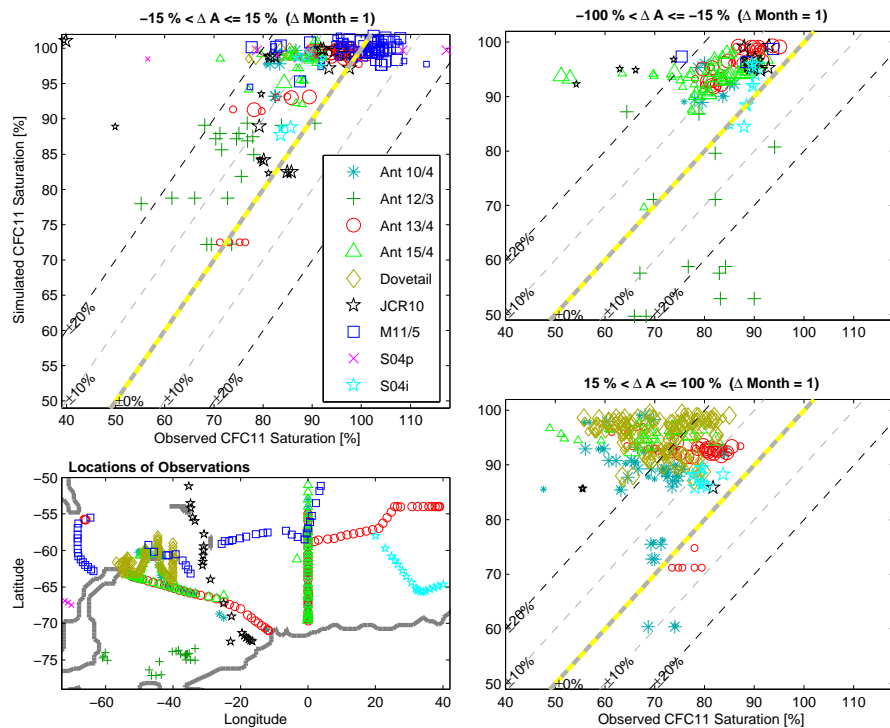
12

Figure 4: Observed vs. simulated CFC11 saturations restricted to casts with sea ice concentration differences (ΔA : observation − simulation) of less than 15% absolute as described in the text (upper left). Upper (lower) right depicts the observed vs. simulated saturation for sea ice concentration differences higher (lower) than 15% absolute. Large symbols represent depths less than 20 m while small symbols depict deeper observations (20 m–55 m). Locations of the casts are presented in the lower left figure.
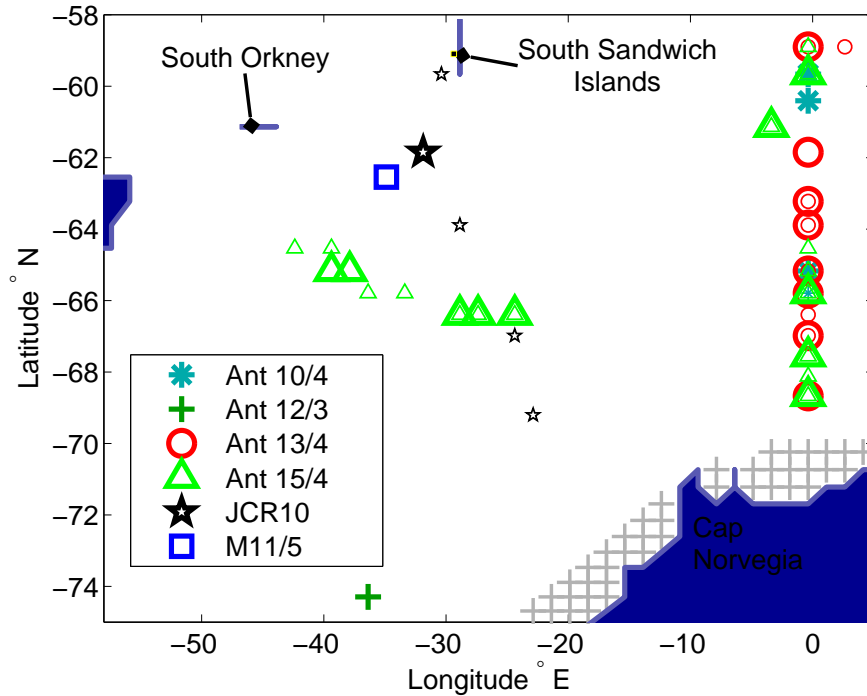
13

Figure 5: Spatial distribution of saturation differences (observations - simulations) by less than -10% (simulation is higher), where the sea ice concentration is smaller by more than -15% in the model (values above the upper 10% line in the upper right panel of figure 4). These represents 58 of total 252 differences. Large symbols represent depths less than 20 m while small symbols depict observations between 20 m and 55 m. The mesh along the coast represents ice shelves.

temperature or salinity spread does not exist.

In the simulations, the maximum spread of the CFC concentrations, computed for the period of observations, is only 2.5%, and the corresponding temperature and salinity spreads are 0.24°C and 0.047, respectively (Tab. 2). Furthermore, the observed strong stratification is not reproduced, in particular in the deep basins. This might be caused by the vertical extension of the two uppermost model layers, set to 0.46% and 0.59% of the entire water column. Hence, for a depth of 5500 m in the central basins the two uppermost layers are 25 m and 32 m thick. This coarse vertical resolution together with elevated mixing in shallow layers, due to the representation of wind-induced turbulence, causes smaller spreads compared to the observations.

The discrepancy between observation and simulation is generally higher for deeper samples, which are potentially located in the lower saturated WW. Furthermore, if the upper ocean is highly stratified and if observations are only available at the standard depth of 50 m below the ASW, these observations may insufficiently represent the saturation at the ocean surface. Therefore, our comparison between simulation and
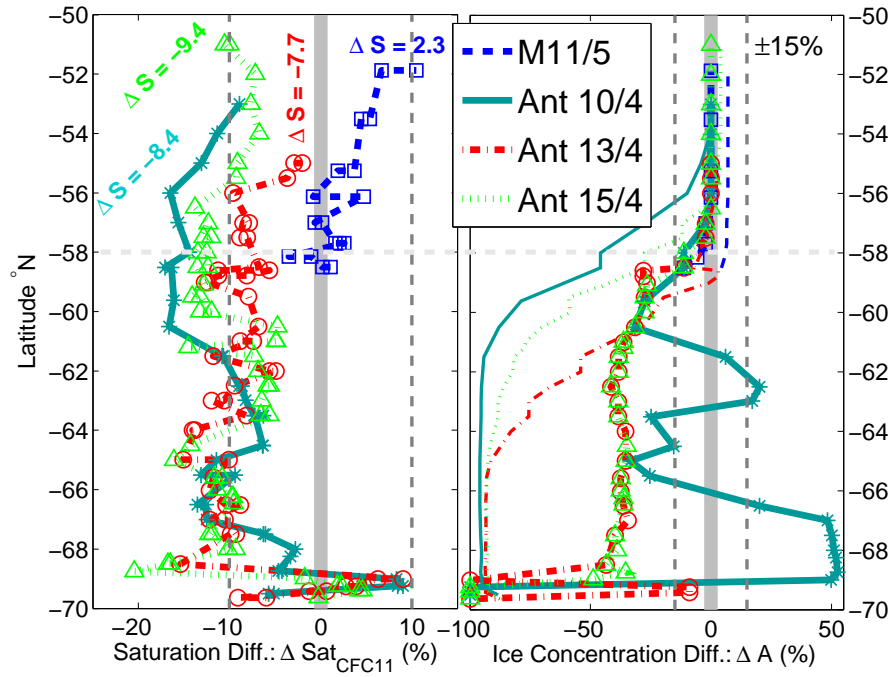
14

Figure 6: Difference between observed and simulated CFC11 saturations (left panel) and sea ice concentrations along the Greenwich Meridian (right panel). The thick (thin) lines represent differences one month prior to (at the time of) the CFC observations. The horizontal dashed line by 58°S corresponds to the northern limit of Figure 5, while the vertical lines are saturation and sea ice concentration differences of $\pm 10\%$ and $\pm 15\%$, respectively. The mean saturation difference of each cruise is indicated by ΔS.

Cruise Name	Date Year	Month	Overall Maximum $\Delta^u s$	$\Delta^u \Theta$	$\Delta^u S$	At max $(\Delta^u S)$ $\Delta^u s$	$\Delta^u \Theta$	At max $(\Delta^u \Theta)$ $\Delta^u s$	$\Delta^u S$	Mean $\overline{\Delta^u s}$	Std $\overline{\Delta^u s}$	Correlation $\Delta^u \Theta$	$\Delta^u S$	No.	PI
ANT XII/3	1995	2–3	16	1.2	0.58	14	0.3	13	0.25	9.5	5.0	24	52	10	WR
M11/5	1990	2–3	12	4.4	0.26	3	0.7	10	0.06	5.8	6.1	76	22	19	WR
WOCE *S04p*	1992	3	38$^{(*)}$	1.3	0.45	39$^{(\#)}$	1.1	31	0.33	25.4	16.4	92	99	3	JB
JCR10	1995	4	29	1.0	0.53	27	1.0	27	0.52	10.2	11.8	57	72	14	AW
WOCE *S04i*	1996	6	6	0.1	0.32	6	0.01	3	0.04	1.2	1.8	30	92	9	WS, MW
ANT XIII/3	1996	4–6	8	0.15	0.13	2	0.06	2	0.03	1.8	1.4	19	16	60	WR
ANT XV/4	1998	4–6	30	0.2	0.90	23	0.24	23	0.90	6.1	8.1	70	92	40	WR
ANT X/4	1992	6–8	16	0.25	0.03	5	0.1	4	0.002	1.5	2.8	38	54	32	WR
DOVETAIL	1997	8–9	6	0.2	0.04	3	0.2	3	0.53	0.7	1.0	20	42	65	WS
Observation	1990–98	2–9	38/30	4.4	0.58	39/27	1.1	31	0.9	3.5	3.8	32	75	252	
Simulation	1990–98	2–9	3	0.2	0.05	2	0.2	3	0.04	0.1	0.06	67	78	252	

Table 2: List of considered data sets (cruises) for model validation and spreads based on at least two observations in profiles of the water column's upper 55 m. The columns show spreads of the CFC11 saturation $\Delta^u s$, potential temperature $\Delta^u \Theta$, and salinity $\Delta^u S$. Compiled are the maximum observed spread (Overall Maximum), regardless of location, and maximum spreads for the cast where salinity (At max $(\Delta^u S)$) or temperature (At max $(\Delta^u \Theta)$) have their maximum spreads. The columns "Mean" and "Std" list for each data set its mean saturation ($\overline{\Delta^u s}$) and the related standard deviation ($\overline{\Delta^u s}$). Correlations are between the deduced CFC11 saturation and temperature or salinity spread of each cruise. The column "No." notes the number of available casts with at least two values; for the WOCE cruises *S04p* and *S04i* we only use a subset of the data sets. The difference between CFC11 and CFC12 saturation spread is mostly within 5% and always below 9% except for the two marked cases for WOCE cruise *S04p*. Here, CFC11 and CFC12 saturation spreads are: $^{(*)}$ CFC12: 28% and $^{(\#)}$ CFC12: 22%. The last column "PI" lists the principle investigators (AW = A. Watson, JB = J. Bullister, MW = M. Warner, WS = W. Smethie, WR = W. Roether).

observations, which for some cruises predominantly consisted of deeper observations, might be biased, which might partly explain the deviation between observation and simulation.

3.2.2 Bias in sea ice concentration discrepancy

To address the effects of sea ice concentration further, Fig. 4 shows model-data comparisons like in Fig. 2, but subdivided according to model-observation discrepancies in sea ice concentration (i.e., observation minus simulation) one month earlier (see above). The neglect of sea ice drift should introduce small errors. Strong sea ice concentration gradients are unlikely within large-scale sea ice fields as sea ice and the upper surface waters flow nearly parallel (Kottmeier and Sellmann, 1996), and the rate of displacement is small. The observed mean sea ice drift velocity amounts to 0.2 cm/s = 5.2 km/month (Kottmeier and Sellmann, 1996), except within the coastal current where the velocity reaches 6 cm/s = 155 km/month, corresponding to a displacement of six grid cells in the sea ice concentration data set.

Selecting only data with sea ice discrepancies <15% (Fig. 4, upper left), the CFC saturation discrepancies fall mostly within +10% and -20%, with an average near to -10%. A similar result is obtained for even more negative values of the sea ice discrepancy (Fig. 4, upper right). For more positive sea ice discrepancies (Fig. 4, lower right), however, the saturation discrepancies show a large scatter and average appreciable lower (approximately -20%). During the *DOVETAIL* cruise (1997, month 8–9) the observed sea ice concentration one month prior to sampling was up to 76% higher than in the simulation. Upstream, at the tip of the Antarctic Peninsula, the simulated sea ice cover vanishes earlier than observed, because the model air-temperatures are too high, amplifying sea ice melting and enabling an enhanced CFC uptake of the northward flowing water masses. This causes the simulated CFC saturations to be higher than observed. On the other hand, if the observed sea ice concentration is lower, the corresponding observed saturations are sometimes distinctly higher than the simulated ones, for example in front of Filchner-Ronne Ice Shelf (FRIS) (*ANT XII/3*).

A higher simulated saturation for locations of higher sea ice concentrations seems to contradict our expectation (Fig. 4, upper right). This occurs predominately along the Greenwich Meridian south of the ACC (Fig. 5). One month prior to (Figs. 3 and 6) and at the time of (Fig. 6) the CFC observations, the sea ice concentration in the model is higher than observed. So any sudden local sea ice melting and incipient CFC fluxes can be excluded to account for the difference.

East of the Greenwich Meridian sea ice retreats early and completely during the summer. The region is characterized by the inflow of CFC enriched surface water masses from the year-round ice-free ACC. Since the model does not resolve the frontal system which clearly separates the surface layers of the Weddell Gyre from the ACC, higher saturated surface water masses can penetrate into the gyre at its northern edge. In addition, a tongue of elevated CFC saturated surface waters extends toward the Greenwich Meridian along the Antarctic coast, as it is even seen in a mean field (Fig. 8). In the coastal current the saturation difference increases by some 20% and changes sign under still high sea ice concentrations differences (Fig. 6). Therefore, in the model the inflow of higher saturated surface waters compensates for the expected lower CFC sat-
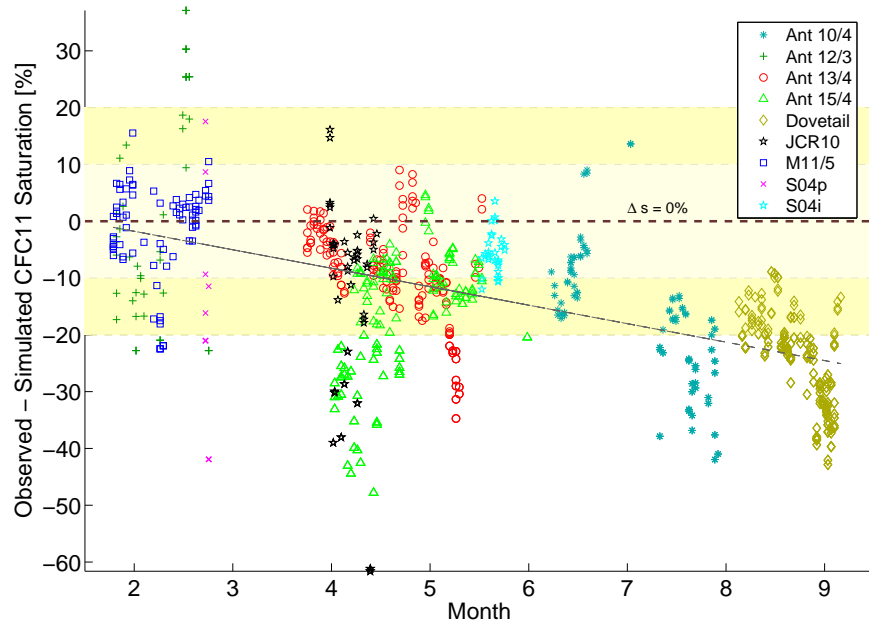
Figure 7: Difference between observed and simulated saturations in the upper 55 m as a function of time (month of year). Colored bands mark deviations between ±10%, and ±20%. The thin line represents the linear trend through all data points (correlation between month of observation and saturation difference is 0.57).
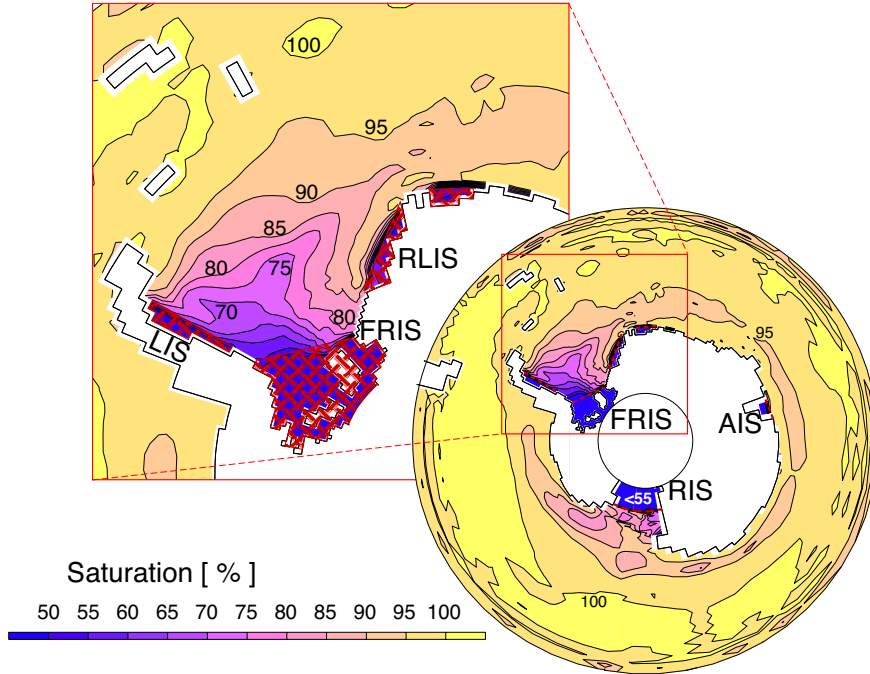
Figure 8: Simulated mean CFC11 saturations in the mixed layer at the time of observations (1990–1998). The Filchner-Ronne (FRIS), Larsen (LIS), Riiser-Larsen (RLIS), Amery (AIS), and Ross (RIS) ice shelves are hatched.

uration under a stronger than observed sea ice cover. This clearly shows the influence of local differences in the CFC-uptake controlling parameter on the difference between observed and simulated saturation and highlights the need to capture adequately the contribution of tracers remotely exchanged between atmosphere and ocean.

A final item is the model/data CFC saturation differences as a function of season (Fig. 7). Beyond appreciable scatter, one finds a trend of lowest discrepancies in austral summer (February) and generally higher ones during the transition from austral winter to spring (August/September), differing by close to 25%. All large differences are related to cruises operating in the northwestern Weddell Sea near the sea ice edge (*ANT X/4* end of July, *ANT XIII/4* end of May,*ANT XV/4* begin of April, *DOVETAIL*). However, at the northern tip of the Antarctic Peninsula the model's sea ice concentration is too low because sea ice melts too early (Timmermann et al., 2002), which permits an unrealistic strong uptake of gaseous tracers causing excessive surface saturations.

3.3 Simulated spatial distribution of the CFC surface saturation

The simulated mean saturations of the surface layer (Fig. 8) are calculated for the period covered by all measurements in Table 2 and represent predominantly summer conditions. A comparison with the observed distribution is given by Rodehacke et al.
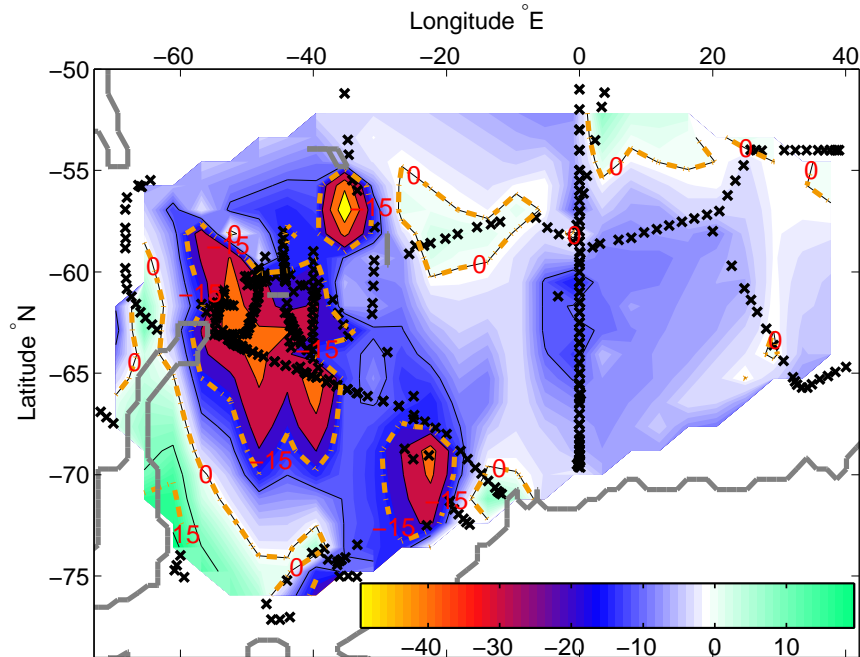
19

Figure 9: Spatial distribution of the difference between observed (1990–1998) and simulated CFC11 saturations in the mixed layer down to 55 m (triangle-linear interpolation of $\Delta \text{Sat}_{CFC11} = \text{Sat}_{CFC11,OBS} - \text{Sat}_{CFC11,SIM}$). The contour interval of thin black lines is 10% and the contours of -15%, 0% and 15% are highlighted by amber dashed-dotted lines. Crosses represent observations and the gray thick lines are the coastlines.

(2007, Fig. 5).

In parts of the Antarctic Circumpolar Current, the mixed layer is saturated by up to 103% (Fig. 8), caused by temperature-related processes (Section 5.1), while in a small band around Antarctica the saturation drops below 95%, emphasizing the retreating winter sea ice. Starting at the Greenwich Meridian, a tongue of higher saturated waters spreads westwards to the southern Weddell Sea. Saturations below 60% cover the area from the Filchner-Ronne Ice Shelf (FRIS) to the Larsen Ice Shelf (LIS) and extend into the central Weddell Sea. Also in front of the Ross Ice Shelf (RIS) saturations are low with 70%–80%. The saturation drops below 55% in ice shelf caverns (Section 4.3). In general, the saturation decreases towards Antarctica, and regions covered with perennial sea ice are characterized by lower saturations.

3.4 Summary of the comparison between observed and simulated CFC saturations

The comparison reveals certain biases between observed and simulated saturations, superimposed on an appreciable scatter. There appears to be a general bias of simulated

20

saturations being too high by about 10 % (Fig. 4, upper left and right; Fig. 9), with the exception of regions with low simulated sea ice concentration compared to the observations (Fig. 4, lower right). These regions appear to be particularly problematic. A seasonal trend also exists (Fig. 7); however, the related observations have been taken at the northern tip of the Antarctic Peninsula known to have too high simulated saturations (Fig. 9), whereby the orange spot northeast of the Antarctic Peninsula is strongly determined by the high density *DOVETAIL* observations (65 observations at this location, Tab. 2, compare Fig. 3, lower left). Sea ice appears to act as a principal control, modulating the ocean's uptake of gases by suppressing the gas fluxes. Therefore, much of the biases and the scatter appear to be related to the sea-ice simulations. Since the model is forced with a recurring seasonal climatological cycle, differences between the actual and climatological sea ice concentration have to be expected.

Since the model uses as a vertical coordinate the terrain-following s-coordinate, layer thicknesses depend on water depth, resulting in a top-layer thickness of up to 25 m in the deep basins. The presence of enhanced wind-induced turbulence homogenizes the concentrations within the two upper-most model layers. This and the inadequate vertical resolution in the deep basins cause an insufficient representation of the separation of the WML into ASW and WW during summer. However, the slightly underestimated mixed layer depth along the Greenwich Meridian (Latitude range $54°$S and $60°$S, Fig. 1) does not cause the detected difference observed and simulated surface saturation. Since for some cruises only observations in the WW layer are available, which are generally lower in saturation than for the top ASW layer, our comparison might be biases by too low reference values. If we (a) restrict the comparison to the upper 20 m, (b) consider differences in sea ice concentration before and at the time of the measurements, and (c) apply an uncertainty of 10%–20%, derived from the CFC saturation spread in the upper 55 m (Figs. 3, 9), we obtain a better match between observation and simulation to a limited degree only. The observed state might be better represented when using a higher vertical resolution and a more sophisticated mixing scheme for the mixed layer. Further sources for errors are the neglect of extremes in the forcing fields and the comparison of point measurements with spatially-averaged simulated values. However, an improvement regarding these points is outside the scope of the present work.

For the Atlantic sector of the Southern Ocean, observed saturations (upper 55 m) taken at section cross-overs show typical differences of 5%–10% absolute in open-ocean regions and of 10%–20% absolute in perennial sea ice covered regions (Fig. 3). This strong variability appears to be controlled by the actual environmental conditions before and during the field measurements. A temporal trend beyond a seasonal variation cannot be extracted from the available CFC observations.

When interpreting the simulations, as addressed in the following, one has to keep in mind the limitations and uncertainties the presented model/data comparison has revealed. However, the comparison showed that the simulations approach reality to a meaningful degree.

4 Seasonal and long-term evolution of the simulated CFC surface saturation

We evaluate the seasonal and long-term temporal evolution of the simulated saturations in the vicinity of the main deep and bottom water formation sites of the Southern Ocean, located in the Ross Sea, Prydz Bay in front of the Amery Ice Shelf (AIS), and southwestern Weddell Sea (Baines and Condie, 1998; Rodehacke et al., 2006, 2007).

4.1 Seasonal cycle of the CFC saturations

For the all-season ice-free areas, the simulated surface saturation shows a distinct seasonal cycle with values between 87% and 105%. Triggered by sea ice formation, the continental shelf in front of FRIS (hereafter called FRIS Shelf; areas are defined in Fig. 10) is homogenized by winter convection, primarily in June and July. This process transports surface waters to greater depth and mixes them with ambient water masses of lower concentration and saturation. On the broad continental shelves deep convection initializes the formation of HSSW, which contributes to the formation of deep and bottom water and causes reduced sub-surface saturations compared to surface values.

Highest amplitudes of the seasonal saturation cycle exist in front of FRIS and RIS (Tab. 3, Fig. 11a, d). For the FRIS Shelf, the CFC11 saturation varies at the surface and in the whole water column by 28% and 2% (Tab. 3), respectively (simulated surface values are those of the top layer, while whole water column denotes a grid box volume weighted top-to-bottom average). In the Ross Sea, the corresponding values amount to 66% and 2%, respectively. The high surface value is due to the strong seasonal cycle of sea ice concentration combined with convection, which entrains low saturated water masses into the surface layers. The maximum saturation overlaps in time with an increasing sea ice concentration that stops a further relaxation of the concentration disequilibrium (Fig. 11a–d). In general, the saturation reaches its maximum two month after the sea ice concentration minimum (Fig. 11a–d).

From September to November the surface layer and water column saturations in front of FRIS are virtually equal, because during winter water mass transformation homogenizes the water column (Fig. 11a). In front of RIS the surface layer values fall even below the water column mean (Fig. 11d), because low saturated water masses, which flow out of the RIS cavern, are mixed into the surface layer. As will be discussed for the FRIS cavern below (Sec. 4.3), the saturation of water masses decreases while passaging through the cavern with inflow at the bottom and outflow in the upper layers (Fig. 14). Since a high sea ice concentration in the southern Ross Sea during winter inhibits CFC uptake from the atmosphere (Fig. 15), the flow of water masses from the RIS cavern into the (open ocean's) surface layer reduces its saturation below the corresponding water column mean.

The seasonal evolution is different for the areas Weddell Sea I/II and Prydz Bay. A large fraction of the water column of Weddell Sea I/II is not directly ventilated and remains mostly stratified during the year. Here, a significant fraction of the water column is characterized by old and, hence, less saturated water masses. These are ventilated by slow diffusive transports (mixing) either from regions of deep convection,
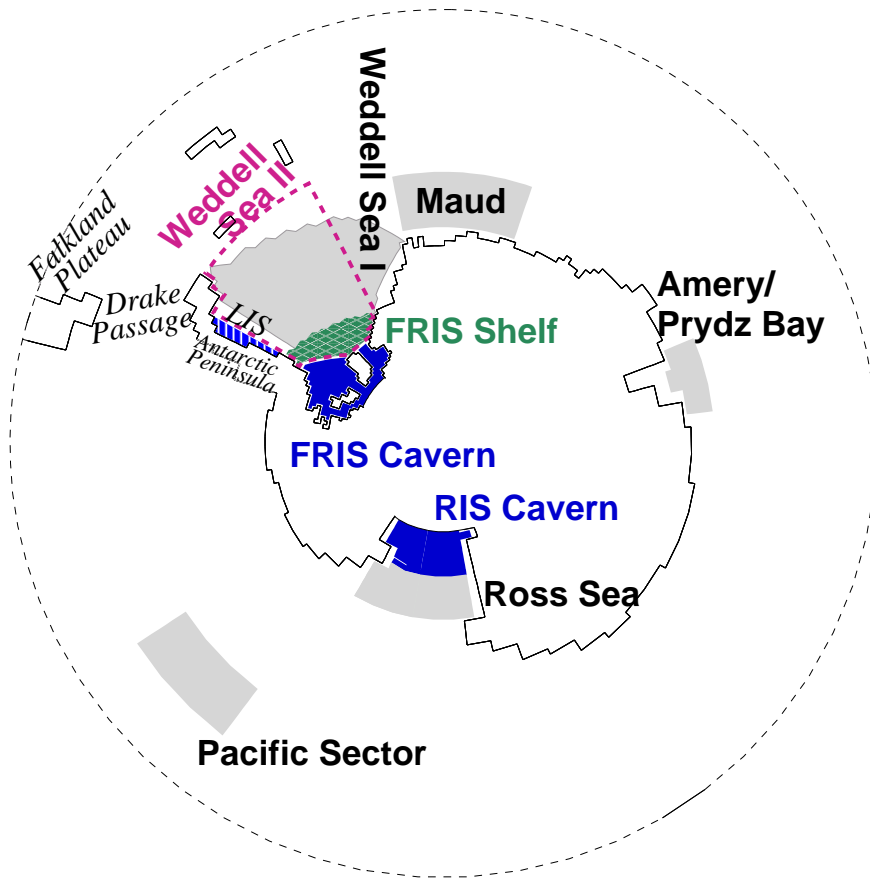
22

Figure 10: Definitions of selected areas and locations mentioned in this study. The areas Weddell Sea I (grey area) and Weddell Sea II (dashed red line) both comprise completely the FRIS Shelf area (green hatched). Dark blue areas represent ice shelf caverns, FRIS: Filchner-Ronne Ice Shelf, RIS: Ross Ice Shelf, LIS: Larsen Ice Shelf. Additional areas like Maud Rise, Amery/Prydz Bay, Ross Sea, and Pacific Sector are shown in grey.

Area	Surface				Water column		sea ice conc.	
	$\overline{s}_{\text{CFC11}}$ [%]		$\overline{s}_{\text{CFC12}}$ [%]		$\overline{s}_{\text{CFC11}}$ [%]		$\overline{A}$ [%]	
	min	max	min	max	min	max	min	max
FRIS cavern	31	32	29	30	33	34	100	
FRIS shelf	47	75	45	73	45	47	65.9	96.3
Weddell Sea I	64	86	62	85	35	36	46.1	96.4
Weddell Sea II	69	85	67	84	35	36	50.3	95.7
RIS cavern	25	27	24	26	29	29	100	
Ross Sea	25	91	24	90	30	32	20.3	96.0
Prydz Bay	40	95	40	94	22	34	4.83	94.0
Total surface	83	97	82	97	47	62	5.52	30.2

Table 3: Extreme values of seasonal (1995) mean CFC saturation for the surface and whole water column in selected areas together with maxima and minima of the spatial mean sea ice concentration $\overline{A}$. CFC11 and CFC12 saturations are virtually identical for the whole water column (Fig. 11a–d). Areas are defined in figure 10 and text.

like the FRIS Shelf, or from the Antarctic Coastal Current as described for the Weddell Gyre by Hoppema et al. (2001).

In the model, the Prydz Bay area is continuously flushed by the coastal current, which carries freshly ventilated waters from sources like the Ross Sea, Wilkes Land, and Adélie Coast (Rodehacke et al., 2006, 2007). Since sea ice retreats relatively early upstream of Prydz Bay, the surface layer comes relatively close to equilibrium during summer (Fig. 8, 11c). Enhanced coastal Ekman pumping in the Indian Ocean (Fig. 16), driven by katabatic winds, and winter convection triggered by sea ice formation both ventilate also deeper levels of the coastal current. However, the missing seasonal cycle in the deep water column and a negligible long-term trend (Sec. 4.2) indicate that a constant supply of older water masses overwhelms the surface influence and reduces the seasonal-cycle amplitude at depth.

The saturation of the "Total surface" in Tables 3 and 4 are the grid box volume weighted mean of either all ocean surface grid boxes (table column: Surface) or all grid boxes from the surface to the bottom (table column: Water column). In summer the high saturation of the total surface has three causes. a) Since the sea ice retreats considerably during summer around Antarctica (e.g. Gloersen et al. (1992)), the mean summer sea ice concentration is low (Fig. 15). This permits an enhanced CFC uptake (Fig. 15), in particular, in the transition zone between the year-long ice-free ACC and Antarctica's margin. b) For northern grid boxes the mixed layer reaches an equilibrium concentration in summer (Fig. 8), because stable summer stratification suppresses water mass exchange with lower saturated deeper layers. c) Since the volume ratio of the grid boxes at latitudes $50°$S:$65°$S:$70°$S is 1.88:1.2:1, the northern higher saturated boxes dominate the volume weighted mean.

Along the path of freshly ventilated water masses from the Filchner Trough to the South Sandwich Islands, the seasonal cycle is only pronounced near the deep and bottom water formation sites (Fig. 12), where also the saturation is highest. A detailed
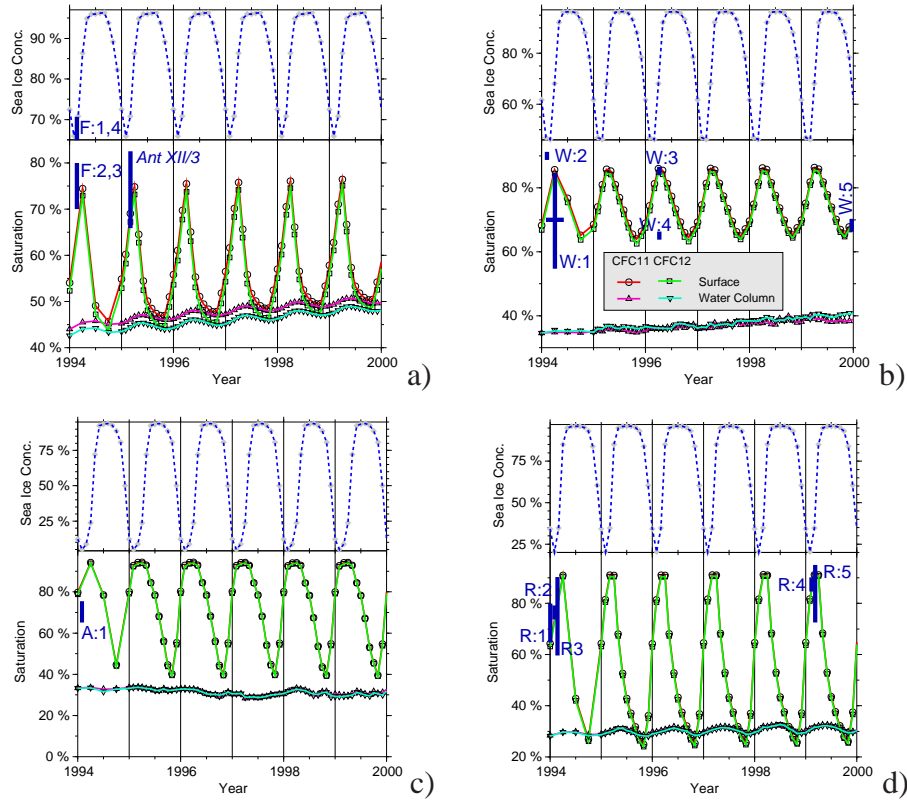
24

Figure 11: Seasonal cycle of the simulated CFC11 and CFC12 saturations for the surface (top model layer) and water column (a) in front of FRIS, (b) the Weddell Sea II, (c) Prydz Bay, and (d) the Ross Sea. For each region the upper panel shows the temporal evolution of the sea ice concentration. Please note the different scales for sea ice concentration and saturation. Observations are depicted by vertical bars (range of values), where *Ant XII/3* is in front of FRIS and represent its mean value and standard deviation (Tab. 2). The abbreviations for the other cruises are listed in Table 1. If values are outside of the time axis, they have been adjusted by applying the simulated linear annual mean saturation increase (Tab. 4).

description of the spreading of CFC-containing, freshly ventilated waters is given by Rodehacke et al. (2007). Further downstream and down the continental slope (beyond station 10 in Fig. 12) the saturation drops. The enhanced seasonal cycle and the slightly elevated seasonal mean saturation between position 20 and 28 are related to the formation of water masses in front of LIS, which is confirmed by independent observations (Huhn et al., 2008; Fahrbach et al., 1995; Weppernig et al., 1996). The seasonal cycle vanishes and the saturation settles to a constant value of about 35% as the flow reaches the northern tip of the peninsula and advances to the South Sandwich Islands.

25
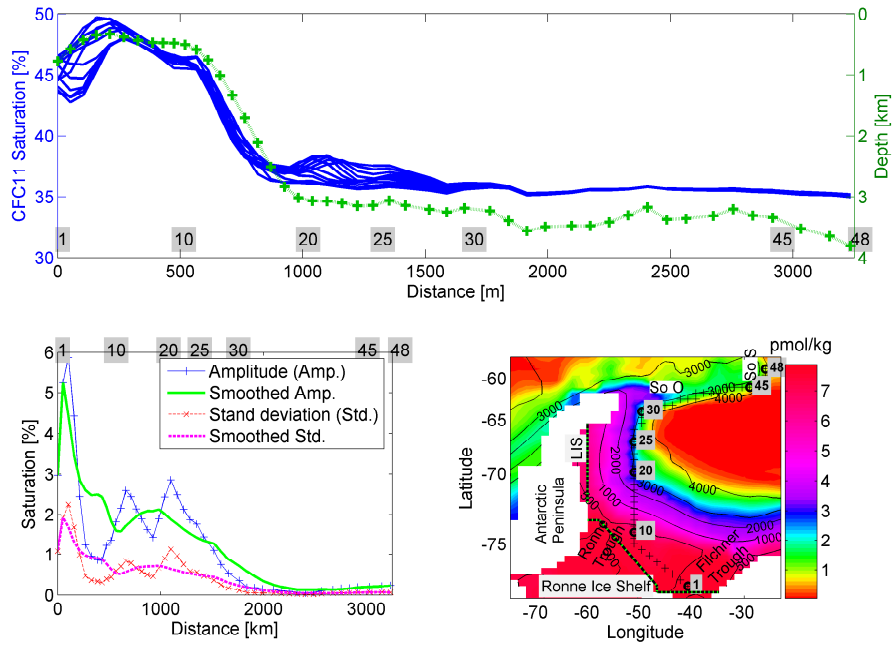
Figure 12: Simulated path of freshly ventilated water masses and the seasonal saturation cycle in the Weddell Sea bottom layer in 1998. The upper panel shows the CFC11 saturation for each month in the bottom layer (solid lines) and the corresponding layer depth (green line). The lower left panel depicts the seasonal amplitude (maximum - minimum) of the saturation along the path (original and smoothed with a 15-points moving average) and the standard deviations (see embedded legend). The lower right panel shows the distribution of CFC11 concentration in the bottom layer of the south/western Weddell Sea with depth contours 500, 1000, 2000, 3000, and 4000 m. In all panels numbers in grey squares represent positions along the path. LIS: Larsen Ice Shelf, So O: South Orkney Island, So S: South Sandwich Islands.

Area	s_{CFC11} [%]		$\overline{\Delta s_{\text{CFC11}}}$	s_{CFC12} [%]		$\overline{\Delta s_{\text{CFC12}}}$	$\overline{s_{\text{CFC11}}^{\text{offset}}}$	$\overline{s_{\text{CFC12}}^{\text{offset}}}$
Year	1990	1998	$[\frac{\%}{\text{year}}]$	1990	1998	$[\frac{\%}{\text{year}}]$	[%]	[%]
FRIS cavern	23.7	35.1	1.4	23.7	32.9	1.2	0.7	0.7
FRIS shelf	50.2	57.0	0.9	49.3	55.1	0.7	0.2	0.2
Weddell Sea I	66.0	69.6	0.5	65.2	68.6	0.4	5.4	5.5
Weddell Sea II	68.6	72.4	0.5	67.9	71.4	0.4	4.2	4.3
RIS cavern	22.2	27.2	0.6	22.1	26.7	0.6	0.3	0.2
Ross Sea	63.6	64.6	0.1	62.6	63.6	0.1	-10.3	-9.9
Prydz Bay	79.0	80.0	0.1	78.2	79.2	0.1	-6.3	-5.9
Total surface	88.8	89.6	0.1	88.5	89.3	0.1	1.0	1.1

Table 4: Simulated mean CFC saturations s_{CFC} at the surface for selected areas in January for the years 1990 and 1998, i.e., in the southern-hemisphere summer. $\overline{\Delta s_{\text{CFC}}}$ is the mean rate of change per year. The yearly mean saturation can be obtained by adding $\overline{s_{\text{CFC11}}^{\text{offset}}}$ or $\overline{s_{\text{CFC12}}^{\text{offset}}}$, respectively, to the presented January-1-saturations s_{CFC}. The offset is based on the year 1998; the temporal evolution of the offset is negligible for the period 1990–1998 (Fig. 11).

4.2 Long-term evolution of the CFC saturation

The simulated saturations are rising steadily, apart from somewhat variable values prior to 1950 (Fig. 13). The near-exponential growth of the atmospheric concentrations after 1960 coincides with a reduced increase of the surface saturations, which grew again around 1978 when the atmospheric rate of increase became nearly linear. After 1990 (1995) the atmospheric CFC11 (CFC12) concentrations approached a constant level which induced even slightly higher saturation growth rates in the surface layer.

Early on, the CFC12 saturation exceeded that of CFC11 because CFC11 was released to the atmosphere several years later (1937 vs. 1946) (Walker et al., 2000) so that its relative growth rate was larger, but during the 1970s the differences vanished.

Saturation growth rates (Tab. 4) are high where surface concentrations are low, often related to a compact ice cover (FRIS and RIS caverns) or to high, year-round sea ice concentrations (FRIS Shelf; Fig. 11, Tab. 3) that impede air-sea exchange. Another factor might be the mixed layer entrainment that brings tracer-poor water to the surface. The latter reduces the concentration and saturation at the surface, both controlled by growing atmospheric tracer concentrations up to the turn of the millennium.

The comparison of the simulated surface saturations with observed ones (Tab. 1) reveals that in front of FRIS the latter are (slightly) higher than simulated. However, in 1985 the observed sea ice concentration (Gloersen et al., 1992) was partly less than the average sea ice concentration that drives our model, which allowed exceptional high saturations of 85% (Mensch et al., 1996) compared to simulated of approximately 50%. The observed saturation in the central Weddell Sea is captured by the model for both Weddell Sea I/II, although we compare point measurements, which range from 65% to 90%, with simulated areal means. The observed saturation of 35% in the Filchner Trough (Schlosser et al., 1991) and the late summer surface CFC11 saturations in the
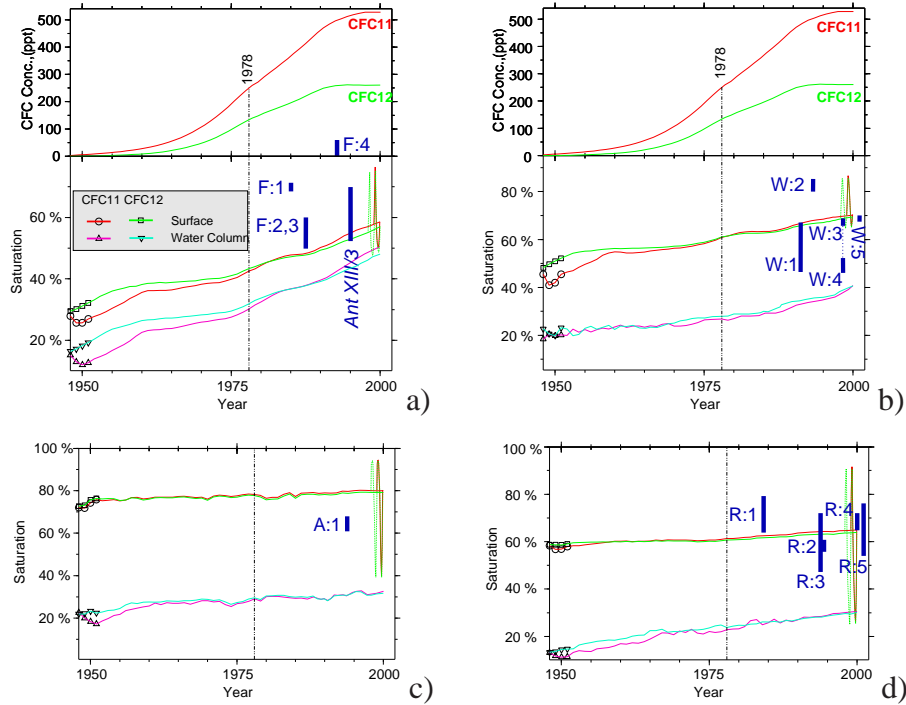
27

Figure 13: Long-term temporal evolution of the CFC11 and CFC12 mean saturation for (a) in front of FRIS, (b) the Weddell Sea II, (c) Prydz Bay, and (d) the Ross Sea. In (a) and (b) the upper panels show the temporal evolution of atmospheric CFC concentrations. Saturations are given at the turn of the year. One (two) seasonal cycle(s) of CFC11 (CFC12) surface saturation are inserted for comparison; see also Figure 11. Please note the different scales for saturation and the additional information in Table 4. Observations (e.g.) are depicted by vertical bars and marked according to the abbreviations in table 1 (cf. Fig. 11). Since the curves are based on January values, the observationes of other months (predominantly in February) have been adjusted by the simulated saturation difference between the time of observations and January: F:1,2=14%, F:3,4,5=18%, W:1=11%, W:2=6%, W:3,4=18%, W:5=0%, A:1=9%, R:1,5=0%, and R:2,3,4=18% (Fig. 11).
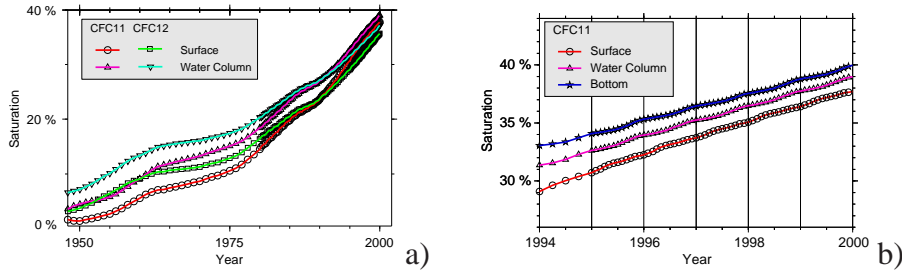
Figure 14: Temporal evolution of mean CFC11/12 saturation within FRIS; (a) long-term evolution (after 1980 the seasonal cycle is added), (b) higher resolved temporal evolution CFC11 of surface, water column, and bottom layer saturations.

Ross Sea of 72%–95% in 2000/2001 (Rivaro et al., 2004) also agree with our simulated values of 68%–91% for the period February-1999 to May-1999 (Fig. 11d) even if we add the deduced trend (Tab. 4) of 0.1%/year. Additional summer saturations (Tab. 1, Smethie and Jacobs (2005)) observed in the Ross Sea range from 64% (CFC11) to 79% (CFC12) in January/February-1984 (February-1994: 74%–79% and February/March-2000: 84%–90%). These values are reproduced by our simulated CFC11 and CFC12 saturations of 61%–79% in January/February 1984, 78%–80% in February 1994, and (extrapolated from January 2000) 82%–92% in February/March 2000.

4.3 Saturation beneath the Filchner-Ronne Ice Shelf

Weddell Sea shelf water masses carry the CFC signal into the FRIS cavern driven by the so-called "ice pump" (Lewis and Perkin, 1985). The CFC saturation and its seasonal cycle are largest near the bottom indicating that the model inflow occurs mainly at depth (Fig. 14b), which is in agreement with hydrographic observations of Nicholls (997a); Nicholls et al. (2001); Nicholls and Makinson (1998). The inflow mixes with water masses of lower CFC concentration/saturation. At shallower depth the reduced amplitude of the seasonal cycle and the lower saturation both characterize an outflow which is a mixture of different water masses formed at previous times with lower saturations. The FRIS cavern shows the highest mean saturation growth rate of 1.4%/year (Tab. 4), which even exceeds the corresponding seasonal cycle of 1% (min–max) absolute (Tab. 3).

5 Discussion

To understand the processes governing the simulated saturations we inspect the CFC uptake fluxes. First we describe qualitatively the spatial distribution of the CFC fluxes during the year. We also investigate processes which can potentially cause high fluxes and complete the flux analysis by presenting correlations between fluxes and thirteen parameters. Ultimately, we show to what degree the assumption of a constant saturation instead of the simulated temporal evolution can cause erroneous results by inspecting
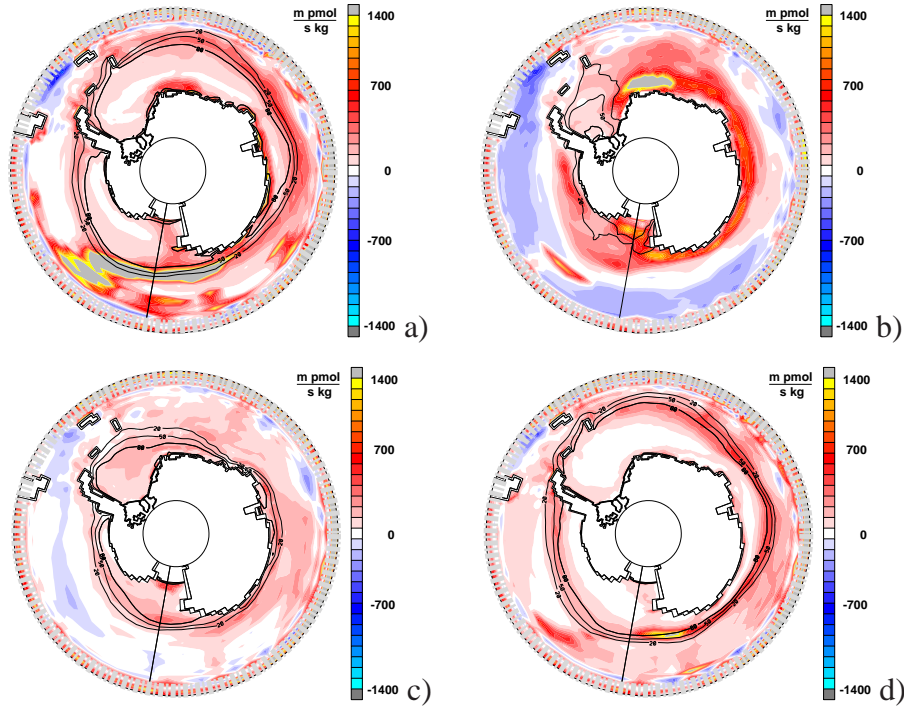
29

Figure 15: Monthly means (October, January, April, and July) of CFC11 fluxes (m pmol/s/kg) for model year 1999–2000; (a) spring, (b) summer, (c) autumn, and (d) winter conditions (positive = uptake, flux into the ocean). The black contour lines represent the sea ice concentration of 20%, 50%, and 80% for the considered month. The blurred ring masks the model's northern buffer zone.

exemplarily deep/bottom water formation rates based on tracer inventories

5.1 CFC-Flux and its dependence on physical parameters

Wherever dense surface water masses sink and are replaced by low-concentration/saturation sub-surface water masses, a surface saturation below the equilibrium is produced, which supports a CFC flux. Therefore, high CFC fluxes mark areas where deep and bottom water might be formed or intermediate water might be subducted.

The flux in the southeastern Pacific west of Drake Passage is driven by the seasonal cycle of the sea surface temperature (SST). Rising summer temperatures reduce the equilibrium concentration so that saturated water masses become supersaturated. This triggers a CFC escape flux from the ocean to the atmosphere (Fig. 15). Conversely, declining SST during winter increases the equilibrium concentration, supporting a flux from the atmosphere into the ocean.

Sea ice formation triggers convection and thus downward transport along Antarctica's periphery, resulting in a distinct seasonal cycle of the saturation in the mixed

30
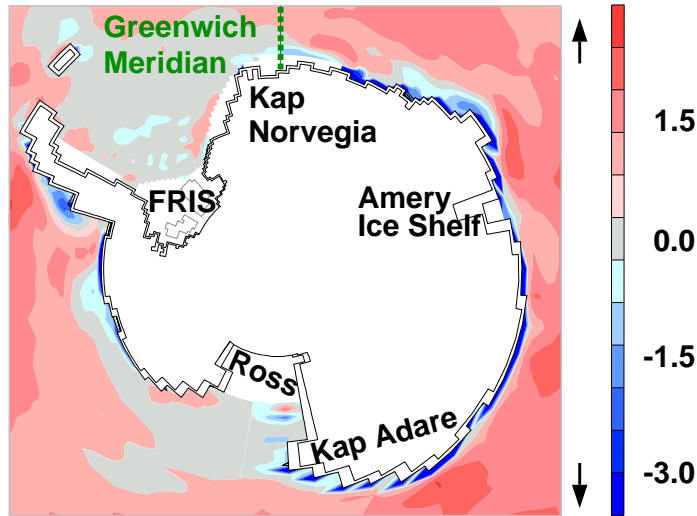
Figure 16: Seasonal mean of Ekman force (transport). Positive values indicate upwelling, unit $1\frac{\text{g m}^2}{\text{s}} = 10^{-3}\text{N}$.

layer (e.g., Fig. 11). The downwelling is amplified by a year-round Ekman transport (Fig. 16) which is, however, minor in some coastal areas of the Pacific Ocean.

5.1.1 Correlation between CFC fluxes and environmental parameters

The CFC flux is controlled by a complex interplay of several processes. Table 6 lists correlations between potentially relevant parameters and the simulated CFC fluxes. These are based on calendar month-means averaged over simulated properties of the years 1998–2000.

The Pacific sector (cf. Fig. 10), located far away from Antarctica, is characterized by a high correlation between CFC uptake and SST (Fig. 17). The exceptional high CFC variability compared to surrounding areas (Fig. 15) is influenced by advective flow across the 100–m depth level (mixed layer depth: 75–150 m). The upwelling rate (44 cm/day in January – 47 cm/day in June) is driven by the sea surface salinity (SSS), which is controlled by the fresh water/salt fluxes (correlation between salt flux and SSS -0.73). The upwelling seems to be amplified by wind-induced Ekman transport in the months March–June, but its correlation with CFC11 (CFC12) flux is only 0.46 (0.47). We conclude that the CFC fluxes in the Pacific sector are driven by the seasonal cycle of the SST, shifting the surface saturation (correlation -0.83), and by the water mass exchange across the pycnocline, caused by the salt flux at the ocean surface (Fig. 17).

At Maud Rise, the spring melting of sea ice initiates a high CFC flux into the undersaturated surface waters. The correlation between CFC flux and SSS rates or salt flux (Fig. 18) are -0.93 and +0.81, respectively (Tab. 6). Maud Rise is located at the transition between westerly and easterly winds. The divergence brings low-saturated deep waters into the mixed layer year-round supporting the disequilibrium. This is con-

31
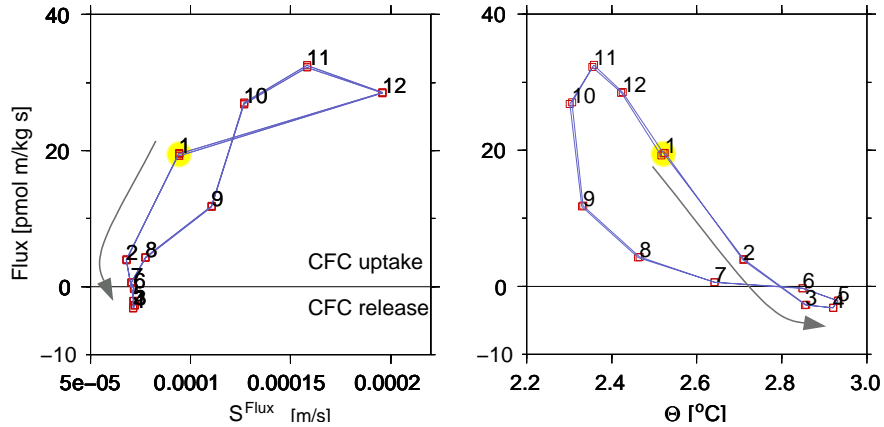
Figure 17: CFC11 flux across the atmosphere-ocean interface vs. salt flux (S^{Flux}, left) and surface temperature (Θ, right) for the Pacific sector for 1998–2000. The arrows indicate the sense of temporal evolution while the small numbers at the data points indicate the month (1 represents January).

firmed by the multi-linear regression analysis, because 95% of the CFC11 variability is explained by SSS changes, wind velocity, mixed layer depth, and its temporal evolution (Tab. 5). However, the correlation between CFC11 (CFC12) saturation and wind velocity amounts to only 0.08 (0.1). Apparently, high sea ice concentrations minimize CFC fluxes and thus maintain the existing undersaturation at the surface caused by the upwelling of deep water masses. After the sea ice melted, high CFC fluxes persist (see Section 4.1) until sea ice growth again suppresses the gas exchange. This is confirmed by independent simulations of the complex flow regime at Maud Rise (Beckmann et al., 2001) and by observed upwelling of subsurface water masses (Muench et al., 2001).

For a subset of the parameters, which are assumed to be linear independent, a multi-linear regression analysis (von Storch and Zwiers, 2003) was performed to determine the order of the multiple parameters and the extent to which they can predict the simulated variability (Tab. 5). The single parameter of highest regression is first determined and then we add consecutively the parameter which causes the strongest increase in regression (Fig. 19). Since we consider the combined effect of the most important parameters and a constant element, the order should be different to the one of decreasing correlations, because the latter describes the strength of the linear relation between the CFC flux and a single parameter.

For the FRIS Shelf the CFC flux is highly correlated with the surface salinity and thus surface density, because for low temperatures the surface density is determined by the SSS. Upwelling (advective flow) across the 100–m level and sea ice concentration exhibit the second largest correlation (Tab. 6). The multi-linear regression of the three most important parameters — salinity, temporal temperature changes, and sea ice concentration — explains 98% of the simulated CFC variability (Tab. 5). For Weddell Sea I the correlation with sea ice concentration is highest, even higher than on the FRIS Shelf. The second highest correlation exists for surface salinity. In contrast,
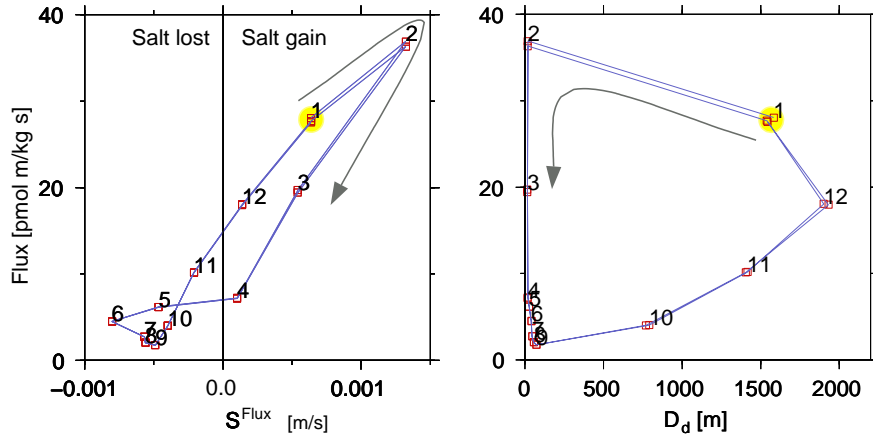
32

Figure 18: CFC11 flux across the atmosphere-ocean interface vs. salt flux (S^{Flux},left) and mixed layer depth (D_d, right) for Maud Rise (1998–2000). The arrows indicate the sense of time evolution, while the small numbers indicate the months.

Weddell Sea II shows the highest correlation with the vertical advective transport and with the temporal evolution of the SST. This indicates the model's ability to reproduce the observed upwelling of Warm Deep Water (WDW) in the central Weddell Sea (Orsi et al., 1993). The latter is confirmed by the multi-linear regression of the four leading parameters — temporal temperature changes, SSS, and the mixed layer depth and its temporal evolution (Tab. 5) — which explains 97% of the variability.

The main difference between Weddell Sea I and Weddell Sea II is that the former covers the area in front of the Riiser-Larsen Ice Shelf where at the beginning of spring a tongue of higher saturated surface water advances toward FRIS (Fig. 8). Weddell Sea I undergoes a higher variability in the sea ice concentration $\overline{\Delta A}$ = 50.3%, which causes a higher seasonal variability in its saturation $\overline{\Delta s}_{\mathrm{CFC11}}$ = 22% (Weddell Sea II: $\overline{\Delta A}$ = 45.4%, $\overline{\Delta s}_{\mathrm{CFC11}}$ = 16%). The multi-linear regression for Weddell Sea I indicates as the decisive parameters, sea ice concentration and its temporal evolution, which account for 90% of the variability. It also confirms the difference in the relation between saturation and sea ice concentration variability between Weddell Sea I and II.

In the Ross Sea the CFC flux is controlled primarily by the evolution of the SST and, secondly, by the mixed layer depth, sea ice concentration, or salt flux. An increasing mixed layer depth is accompanied by the entrainment of deeper, lower-concentrated waters. The temporal evolution of the mixed layer depth is triggered by changes of the mixed layer density (preferably via salinity). The multi-linear regression analysis also determines the evolution of the SST as most significant followed by sea ice concentration, the vertical velocity across the 100–m depth level, and temporal changes of SSS (96% variability).

Since salinity only has a minor effect on the CFC equilibrium concentration, its main effect is to induce density changes. These trigger convection that entrains lower-saturated waters into the mixed layer and causes salinity to be highly correlated with the
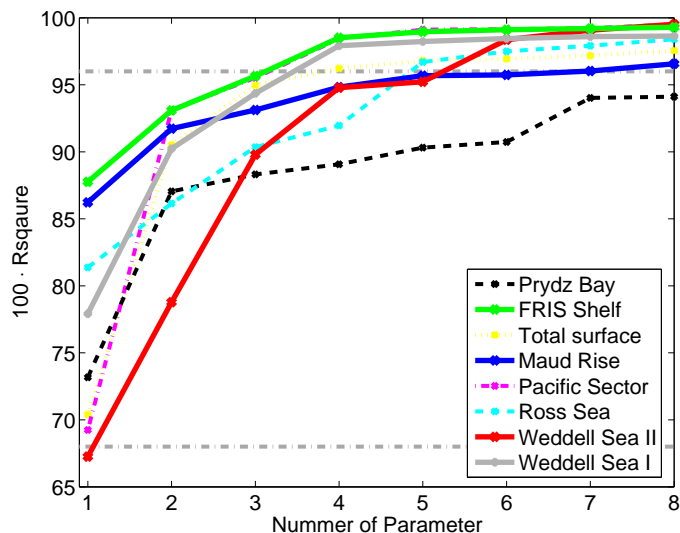
33

Figure 19: Rsquare of multi-linear parameter analysis versus number of considered parameters (Θ, S, $\partial\Theta/\partial t$, $\partial S/\partial t$, D_d, A, $\partial D_d/\partial t$, $\partial A/\partial t$, $w_{100\mathrm{m}}$, $u_{10\mathrm{m}}^2$, $\nu_{\Theta,S}$) which account for the CFC11 flux variability. The horizontal dashed lines mark levels of 66 and 96. For each curve is the order of the considered parameters given in Tab. 5. Please see text for further details.

CFC flux. If we would restrict the multi-parameter regression analysis to parameters detectable by satellite — magnitude and temporal evolution of SST (Barron and Kara, 2006), SSS (Michel et al., 2005; Maes and Behringer, 2000), A (sea ice concentration, Spreen et al. (2008); Comiso et al. (1997)) as well as $u_{10\mathrm{m}}^2$ (wind velocity, Bentamy et al. (2003)) — and if their measurement precisions would be high enough, we could infer 79%–99% of the simulated CFC11 flux variability. Further studies, however, have to be performed to verify the potential of satellite based flux estimates, which is beyond the scope of this article.

5.1.2 Comparison of CFC fluxes with published simulated distributions

A validation of modeled CFC fluxes proves to be difficult because measurements are virtually unavailable so that we have to restrict a comparison to available ocean general circulation model (OGCM) simulations. However, since these provide an inconsistent picture of the spatial distribution of fluxes and their rates, we restrict ourselves to a qualitative comparison.

The most comprehensive account is found in Dutay et al. (2002), who compare the CFC distributions in thirteen global OGCMs. These models exhibit high fluxes in similar areas of the Pacific and at the periphery of Antarctica like in our model, but differences in the spatial distribution and strength are substantial. In fact, the majority of the models show high fluxes at the same locations as our model.

34

Nr	FRIS Shelf		Weddell Sea I		Weddell Sea II		Maud Rise		Ross Sea		Prydz Bay		Pacific Sector		Total surface	
1	S	87.8	A	77.9	$\frac{\partial \Theta}{\partial t}$	67.3	$\frac{\partial S}{\partial t}$	86.2	$\frac{\partial \Theta}{\partial t}$	81.4	$\frac{\partial S}{\partial t}$	73.2	Θ	69.2	D_d	70.4
2	$\frac{\partial \Theta}{\partial t}$	93.1	$\frac{\partial A}{\partial t}$	90.2	S	78.8	$u^2_{10\mathrm{m}}$	91.7	A	86.1	$\frac{\partial \Theta}{\partial t}$	87.0	$\frac{\partial A}{\partial t}$	93.1	A	90.5
3	A	95.7	D_d	94.4	D_d	89.8	D_d	93.1	w_{100}	90.4	$\frac{\partial A}{\partial t}$	88.3	$u^2_{10\mathrm{m}}$	95.5	$\frac{\partial S}{\partial t}$	95.0
4	Θ	98.5	$\frac{\partial \Theta}{\partial t}$	97.9	$\frac{\partial D_d}{\partial t}$	94.8	$\frac{\partial D_d}{\partial t}$	94.8	$\frac{\partial S}{\partial t}$	92.0	A	89.1	w_{100}	98.4	S	96.2
5	$\frac{\partial S}{\partial t}$	99.0	$u^2_{10\mathrm{m}}$	98.2	$\frac{\partial A}{\partial t}$	95.2	$\frac{\partial \Theta}{\partial t}$	95.7	$\frac{\partial A}{\partial t}$	96.7	$\frac{\partial D_d}{\partial t}$	90.3	$\frac{\partial D_d}{\partial t}$	99.1	Θ	96.8
6	$u^2_{10\mathrm{m}}$	99.1	$\frac{\partial S}{\partial t}$	98.5	A	98.4	$\frac{\partial A}{\partial t}$	95.7	$u^2_{10\mathrm{m}}$	97.5	Θ	90.7	S	99.2	$\frac{\partial D_d}{\partial t}$	96.9
7	$\frac{\partial A}{\partial t}$	99.2	$\frac{\partial D_d}{\partial t}$	98.6	$\frac{\partial S}{\partial t}$	99.1	Θ	96.0	$\frac{\partial D_d}{\partial t}$	97.9	D_d	94.0	D_d	99.2	$\frac{\partial A}{\partial t}$	97.2

Table 5: Multiple linear regression analysis between the CFC11 fluxes and eleven parameters. The first row shows for each region the parameter and value of the highest regression (Rsquare, where variability = $\sqrt{\mathrm{Rsquare}}$, 95% confidence) in percentage (%), while the following ones display the added parameter with the total highest regression (cf. Fig. 19). We consider the following parameters: Θ, S, $\partial \Theta/\partial t$, $\partial S/\partial t$, D_d, A, $\partial D_d/\partial t$, $\partial A/\partial t$, $w_{100\mathrm{m}}$, $u^2_{10\mathrm{m}}$, $\nu_{\Theta,S}$, described in the caption of Tab. 6. The gray shaded area marks regression changes by less than 1%, which are insignificant. Please see text for furhter details.

Area	Θ	S	ρ	$\frac{\partial\Theta}{\partial t}$	$\frac{\partial S}{\partial t}$	$\frac{\partial\rho}{\partial t}$	D_d	A	$\frac{\partial D_d}{\partial t}$	$\frac{\partial A}{\partial t}$	$w_{100\,\mathrm{m}}$	u_{10}	S^{Flux}	$\nu_{\Theta,S}$
						Correlation CFC11 Flux								
FRIS Shelf	21^{+23}_{-26}	-94^{+4}_{-2}	-94^{+4}_{-2}	42^{+19}_{-23}	-1 ± 25	-1 ± 25	-64^{+18}_{-13}	-75^{+14}_{-9}	-36^{+24}_{-20}	58^{+15}_{-20}	-76^{+13}_{-9}	24^{+23}_{-26}	4^{+25}_{-26}	38^{+20}_{-24}
Weddell Sea I	18^{+23}_{-26}	-72^{+15}_{-10}	-72^{+15}_{-10}	27^{+22}_{-25}	-54^{+21}_{-16}	-54^{+21}_{-16}	-39^{+24}_{-20}	-88^{+7}_{-5}	-42^{+23}_{-19}	35^{+20}_{-24}	-62^{+18}_{-13}	-35^{+24}_{-20}	24^{+23}_{-25}	19^{+23}_{-26}
Weddell Sea II	33^{+21}_{-25}	-72^{+15}_{-10}	-72^{+15}_{-10}	82^{+7}_{-10}	-36^{+24}_{-20}	-37^{+24}_{-20}	-43^{+23}_{-19}	-77^{+13}_{-9}	-28^{+25}_{-22}	53^{+16}_{-21}	-82^{+11}_{-7}	-36^{+24}_{-20}	3^{+25}_{-26}	27^{+22}_{-25}
Maud Rise	3^{+25}_{-26}	-10^{+26}_{-25}	-10^{+26}_{-25}	-36^{+24}_{-20}	-93^{+5}_{-3}	-92^{+5}_{-3}	27^{+22}_{-25}	-76^{+13}_{-9}	-70^{+16}_{-11}	-55^{+21}_{-16}	41^{+19}_{-24}	67^{+12}_{-17}	81^{+7}_{-11}	65^{+13}_{-18}
Ross Sea	-13^{+26}_{-24}	-20^{+26}_{-23}	-20^{+26}_{-23}	-90^{+6}_{-4}	-73^{+15}_{-10}	-70^{+16}_{-11}	9^{+25}_{-26}	-81^{+11}_{-7}	-83^{+10}_{-7}	-38^{+24}_{-20}	51^{+17}_{-22}	42^{+19}_{-23}	81^{+7}_{-11}	-39^{+24}_{-20}
Prydz Bay	-24^{+25}_{-23}	16^{+24}_{-26}	16^{+24}_{-26}	-46^{+23}_{-18}	-85^{+9}_{-6}	-83^{+10}_{-7}	35^{+20}_{-24}	-49^{+22}_{-17}	-72^{+15}_{-10}	-67^{+17}_{-12}	-19^{+26}_{-23}	-11^{+26}_{-25}	79^{+8}_{-12}	30^{+22}_{-25}
Pacific Sector	-83^{+10}_{-6}	54^{+16}_{-21}	76^{+9}_{-13}	35^{+21}_{-24}	81^{+7}_{-11}	59^{+14}_{-19}	61^{+14}_{-14}	42^{+23}_{-23}	73^{+10}_{-14}	-60^{+19}_{-14}	-44^{+23}_{-19}	22^{+23}_{-25}	71^{+11}_{-15}	3^{+25}_{-26}
Total surface	-78^{+12}_{-8}	72^{+10}_{-15}	74^{+10}_{-14}	17^{+24}_{-26}	-30^{+25}_{-22}	-28^{+25}_{-22}	84^{+6}_{-10}	15^{+24}_{-26}	-28^{+25}_{-22}	-65^{+17}_{-12}	19^{+23}_{-26}	29^{+22}_{-25}	57^{+15}_{-20}	-66^{+17}_{-12}
						Correlation CFC12 Flux								
FRIS Shelf	22^{+23}_{-26}	-94^{+4}_{-2}	-94^{+4}_{-2}	42^{+19}_{-23}	1 ± 25	0 ± 25	-64^{+18}_{-13}	-74^{+14}_{-10}	-35^{+24}_{-20}	59^{+14}_{-19}	-77^{+13}_{-9}	25^{+22}_{-25}	2^{+25}_{-26}	37^{+20}_{-24}
Weddell Sea I	20^{+23}_{-26}	-73^{+14}_{-10}	-73^{+14}_{-10}	28^{+22}_{-25}	-52^{+21}_{-16}	-52^{+21}_{-16}	-40^{+24}_{-19}	-88^{+8}_{-5}	-40^{+24}_{-19}	37^{+20}_{-24}	-64^{+18}_{-13}	-34^{+24}_{-21}	22^{+23}_{-26}	20^{+23}_{-26}
Weddell Sea II	35^{+20}_{-24}	-73^{+14}_{-10}	-73^{+15}_{-10}	82^{+7}_{-11}	-34^{+25}_{-21}	-35^{+24}_{-20}	-44^{+23}_{-19}	-76^{+13}_{-9}	-27^{+25}_{-22}	54^{+16}_{-21}	-82^{+10}_{-7}	-35^{+24}_{-20}	2 ± 25	28^{+22}_{-25}
Maud Rise	2^{+25}_{-26}	-12^{+26}_{-24}	-12^{+26}_{-24}	-34^{+25}_{-21}	-93^{+5}_{-3}	-92^{+5}_{-3}	26^{+22}_{-25}	-77^{+13}_{-9}	-70^{+16}_{-11}	-53^{+21}_{-16}	39^{+19}_{-24}	68^{+12}_{-16}	80^{+8}_{-12}	66^{+12}_{-17}
Ross Sea	-15^{+26}_{-24}	-23^{+26}_{-23}	-23^{+26}_{-23}	-90^{+6}_{-4}	-73^{+15}_{-10}	-70^{+16}_{-11}	8^{+25}_{-26}	-82^{+10}_{-7}	-83^{+10}_{-6}	-36^{+24}_{-20}	49^{+17}_{-22}	43^{+19}_{-23}	80^{+7}_{-11}	-38^{+24}_{-20}
Prydz Bay	-24^{+25}_{-22}	13^{+24}_{-26}	13^{+24}_{-26}	-44^{+23}_{-18}	-86^{+9}_{-5}	-84^{+10}_{-6}	33^{+21}_{-25}	-52^{+21}_{-16}	-73^{+15}_{-10}	-65^{+17}_{-12}	-16^{+26}_{-24}	-10^{+26}_{-25}	9^{+8}_{-12}	30^{+21}_{-25}
Pacific Sector	-83^{+10}_{-7}	55^{+16}_{-21}	77^{+9}_{-13}	36^{+20}_{-24}	80^{+8}_{-12}	58^{+15}_{-19}	61^{+14}_{-19}	41^{+19}_{-15}	72^{+10}_{-15}	-61^{+19}_{-14}	-45^{+23}_{-18}	22^{+23}_{-26}	71^{+11}_{-15}	2 ± 25
Total surface	-70^{+16}_{-11}	60^{+14}_{-19}	62^{+14}_{-19}	31^{+21}_{-25}	-39^{+24}_{-20}	-39^{+24}_{-20}	73^{+10}_{-15}	-1 ± 24	-35^{+24}_{-20}	-62^{+19}_{-14}	-62^{+19}_{-14}	4^{+25}_{-26}	60^{+14}_{-19}	-59^{+20}_{-15}

Table 6: Correlations in percentage (%) of monthly-mean CFC fluxes with properties of the mixed layer for 1998–2000; Θ: sea surface temperature (SST), S: sea surface salinity (SSS), ρ: sea surface density, D_d: mixed layer depth, A: sea ice concentration, $w_{100\,\mathrm{m}}$: advective transport across the 100–m depth level, and u_{10}: 10-m wind speed. S^{Flux} is the salinity flux across the ocean surface (in ice free areas it is salinity times evaporation minus precipitation, $S(E-P)$; in partly ice covered areas the salt input by growing/melting sea ice is included). The vertical mixing coefficient is $\nu_{\Theta,S}$ (Pacanowski and Philander, 1981). Partial fractions are related to $\partial t = 1$ month. The maximum correlation is indicated by a gray box for each area, while correlations higher/lower than 80%/-80% are shown in bold. The 95% uncertainty range of the correlations are presented. The correlations between CFC11 and CFC12 fluxes are between 98.6% (Maud Rise) and 99.99% (Pacific Sector). Areas are defined in Fig. 10.

In the framework of the GOSAC (2002) project cumulative CFC fluxes were determined for the world ocean. High cumulative flux rates were found for the ACC in the Pacific Ocean between the Ross Gyre and the South Sandwich Islands, east of the Greenwich Meridian, and within the Kerguelen Gyre (80°E). Our simulation supports high fluxes east of the Greenwich Meridian and along the southern edge of the Kerguelen Gyre (Fig. 15 b). Our CFC flux estimates for the Pacific sector are also consistent with the results of Hense et al. (2003), who show entrainment of, in their case, nutrient-rich water from below, which leads to the observed phytoplankton bloom (Fig. 6 of Hense et al. (2003)). It is outside the scope of this work to analyze whether satellite detected phytoplankton blooms might be used to assess mixed layer entrainmaint/detrainment and its consequences for gaseous tracers.

We have to consider that some of the models use a salinity restoring to ensure an adequate formation of deep and bottom waters. The choice of the relaxation zones certainly determines the spatial distribution of high CFC uptake regions. In this context, our model results are more plausible than those that use an artificial SSS restoring.

5.2 CFC inventory based deep/bottom water formation rate estimates and their dependence on the temporal evolution of CFC saturations

It is common to assume tracer surface saturations to be time-invariant due to the lack of observation-deduced saturation histories. Since these histories are fundamental for obtaining tracer-based quantities, we address the effect of a neglected temporal evolution by analyzing exemplarily the formation rate of deep and bottom waters based on tracer inventories: $\int c(t)\,dV$. In view of mass conservation, one assumes that the inventory in the abyssal ocean is proportional to both the mean formation rate (P) and the integrated history of the tracer input ($\alpha_S \int \langle S(t)\rangle p_{\text{atm}}(t)\,dt$)):

$$P(t_{\text{ref}}) = \frac{\int c(t_{\text{ref}})\,dV}{\alpha_s \int_{t0}^{t_{\text{ref}}} \langle S(t)\rangle p_{\text{atm}}(t)\,dt}, \tag{3}$$

where α_S is the solubility function, p_{atm} the atmospheric CFC history, and $\langle S(t)\rangle$ the spatial mean saturation at the formation site for time t (e.g., equation on page 94 in Orsi et al. (1999)). The ocean is assumed to be in steady-state and, therefore, temperature, salinity, and ultimately the solubility of the formed water masses do not change and are assumed to be temporal invariant. Since water masses in Antarctica's marginal seas are primarily formed during winter, winter time undersaturations are imprinted as surface water masses are transformed to deep and bottom waters. Therefore, since summer values are improper to describe the conditions during the transformation, only winter conditions can to be considered in the dominator of equation (3).

To estimate the systematic error of this approach, we examine CFC11 in front of FRIS. This area is believed to be the dominant formation site in the Atlantic sector, in which 60% of all Southern Ocean's deep and bottom waters are supposed to be formed (Orsi et al., 1999). The error can be expressed as the ratio of the formation rates, considering a constant saturation $P(t_{\text{ref}}; \langle S(t_{\text{ref}})\rangle = \text{const})$ and the temporal
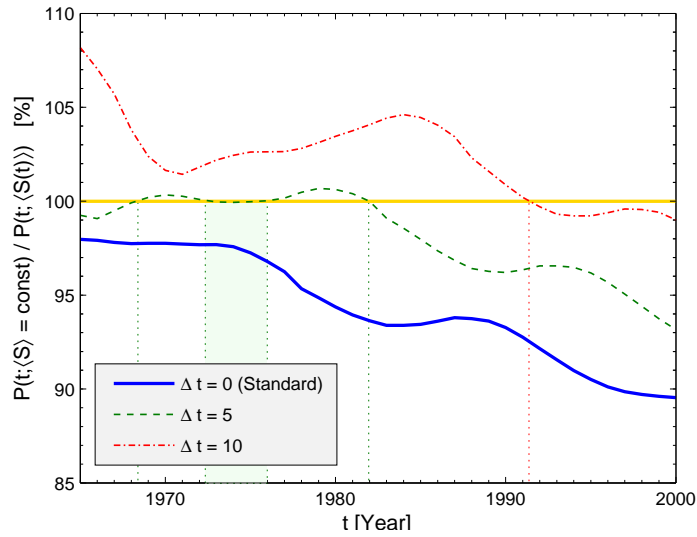
37

Figure 20: Temporal evolution of the ratio of deep water formation rates calculated for a constant saturation at the time of observation/reference t_{ref} and a temporal evolution of the saturation (Eq. 4). CFC11 surface saturation in front of FRIS is considered at the turn of the year (Fig. 13a) starting in t_0=1947 when CFC11 was released to the atmosphere. For the standard run the actual saturation ($\Delta t = 0$) is used while for Δt = 5, 10 years only the saturation is shifted by Δt into the past. Vertical lines and bars highlight the times when both estimates agree.

evolution of $P(t_{\text{ref}}; \langle S(t) \rangle)$:

$$\frac{P(t_{\text{ref}}, \overbrace{\langle S(t_{\text{ref}}) \rangle}^{=\text{const}})}{P(t_{\text{ref}}, \langle S(t) \rangle)} = \frac{\int_{t_0}^{t_{\text{ref}}} \langle S(t) \rangle \, p_{\text{atm}}(t) \, dt}{\langle S(t_{\text{ref}}) \rangle \cdot \int_{t_0}^{t_{\text{ref}}} p_{\text{atm}}(t) \, dt}, \tag{4}$$

where values above (below) 100% represent an over-estimate (under-estimate) of the formation rate.

In the case of a constant saturation we use the simulated value at the time to which the inventory refers (t_{ref}) while in the other case we consider the entire saturation history up to t_{ref} (Fig. 13a). For example, if the reference time is 1998, the atmospheric CFC11 history covers the entire period up to that year, while the constant saturation $\langle S(t_{\text{ref}} = 1998) \rangle$ is 57% (Tab. 4).

We find that ignoring the temporal evolution induces a systematic error of up to 10% for the year 2000. The inventories are always underestimated, but the deviation is smaller at earlier times because their relative atmospheric increases were largest so that much of the tracer was concentrated along the spreading path near to the formation site, i.e., the inventory was very young. The non-linear evolution in Fig. 20 reflects the addition of remotely ventilated waters in the model. The figure also includes results when the saturation refers to a time 5 and 10 years prior to the inventory reference time. Formally, the deviations become lower because the actual saturations increase in time, but the differences between the curves are quite non-linear. For the tracer inventory of 1998, e.g., the saturations were observed 5 (10) years earlier, i.e., in 1993 (1988) with $\langle S(t_{\text{obs}} = 1993) \rangle = 53\%$ ($\langle S(t_{\text{obs}} = 1988) \rangle = 49\%$). However, the selection of a time shift is a rather arbitrary matter.

Other fundamental objections have been raised (Hall et al., 2007) concerning the estimation of formation rates via (4), because it neglects the important role of horizontal mixing. Here, we illustrate the effect of evolving surface saturation on commonly made formation rate estimates. Such evolution would also affect the estimates of the more general 'ventilation-rate distribution' from tracers, as discussed in Hall et al. (2007).

6 Conclusions

Using a regional OGCM, we conducted for the first time a detailed study of the CFC (surface) saturations and the dependence of the CFC fluxes on various parameters for different regions, including the major deep and bottom water formation sites in the Southern Ocean, which are important contributors to the ventilation of the global abyss. We found that the simulated saturations of the surface layer are subject to a pronounced seasonal cycle, and that the time lag between the sea ice concentration minimum and the saturation maximum amounts to two months.

Due to water mass formation by deep convection on continental shelves, the seasonal saturation signal penetrates to great depths. Along the spreading path of the freshly ventilated water masses, the seasonal cycle becomes eroded by mixing and the entrainment of ambient, CFC-poor waters. In addition to the seasonal cycle, all analyzed areas exhibit a significant long-term increase of the surface saturations, 0.1%/year–

0.9%/year (in the 1990s). Near deep and bottom water formation sites, saturation increases are present in the whole water column including the bottom layer, and also further away in the deep and bottom waters as the newly formed waters spread out. The long-term increase of the CFC saturation is strongest within the FRIS cavern (1.4%/year). The increasing atmospheric CFC mixing ratios, suppression of gas exchange by the ice cover, and mixture of freshly ventilated but still undersaturated waters combined with a multi-year composition of very low saturations, cause this strong temporal increase.

In ice-free regions the equilibrium concentration/saturation and hence the flux depends strongly on the SST. When surface water looses buoyancy sufficiently, low-saturation waters are entrained into the mixed layer, triggering a flux from the atmosphere to the ocean. However, areas characterized by high flux rates are not necessarily deep and bottom water formation sites, such as the Pacific sector and Maud Rise.

In ice-covered areas low mixed layer saturations arise from entrainment of low-concentration deep waters while the ice cover suppresses gas exchange. This leads to a strong tracer flux into the ocean when the sea ice retreats. The Maud Rise area demonstrates that high CFC fluxes are not necessarily confined to deep and bottom water formation sites, since here the interaction of the flow with topography lifts deeper water masses to be entrained into the mixed layer.

In summary, sea ice dominantly influences the gas exchange between atmosphere and ocean. Other factors are SST, SSS, salt flux, and mixed layer depth. These parameters can be divided into two groups. SST, SSS, density, and salt flux control the dynamics of the mixed layer, while the mixed layer depth represents a reaction to dynamical processes in an integrated sense. Since the first group of parameters has, in general, the highest correlation with CFC fluxes, a close relation between these fluxes and the formation of deep and bottom waters exists.

Assuming the area in front of FRIS to be representative for the formation of deep and bottom waters (e.g., Weddell Sea Bottom Water, WSBW) in the Southern Ocean, the deep and bottom water formation rates based on tracer inventories are underestimated by up to 10%, if time-invariant instead of realistic (i.e., temporally increasing) saturations are used (Fig. 20). Since the discrepancy increases in (calendar) time, the method using constant surface saturation suggests an erroneous decline of the formation rate with time. Therefore, any noted reduction of water mass ventilation based on tracer inventories should be critically questioned.

Further model studies with an improved representation of the mixed layer should be performed to confirm our results. In addition, a comparison between model runs conducted with climatological and daily forcing should be performed to deduce the influence of varying environmental conditions on the results presented here. Since a realistic tracer input is essential for other deduced properties like transient time distributions (Beining and Roether, 1996; Hall et al., 2002; Waugh et al., 2002), further tracer simulations for all deep and bottom water formation as well as subduction sites should be performed to provide a complete set of CFC surface saturation histories.

References

Asher, W. and R. Wanninkhof (1998). Transient tracers and air-sea gas transfer. *Journal of Geophysical Research 103*(C8), 15939–15958.

Azetsu-Scott, K., E. Jones, and R. Gershey (2005). Distribution and ventilation of water masses in the Labrador Sea inferred from CFCs and carbon tetrachloride. *Marine Chemistry 94*(1-4), 55–66. doi:10.1016/j.marchem.2004.07.015.

Baines, P. and S. Condie (1998). Obervations and modelling of Antarctic downslope flows: A review. In S. Jacobs and R. Weiss (Eds.), *Ocean, Ice and Atmosphere: Interaction at the Antarctic Continental Margin*, Volume 75 of *Antarctic Research Series*, 29–49. American Geophysical Union.

Barron, C. and A. Kara (2006). Satellite-based daily SSTs over the global ocean. *Geophysical Research Letters 33*, L15603. doi:10.1029/2006GL026356.

Beckmann, A., H. Hellmer, and R. Timmermann (1999). A numerical model of the Weddell Sea: Large scale circulation and water mass distribution. *Journal of Geophysical Research 104*(C10), 23375–23391.

Beckmann, A., R. Timmermann, A. Pereira, and C. Mohn (2001). The Effect of flow at Maud Rise on the Sea Ice Cover — Numerical Experiments. *Ocean Modelling 53*, 11–25.

Beining, P. and W. Roether (1996). Temporal evolution of CFC11 and CFC12 concentrations in the ocean interior. *Journal of Geophysical Research 101*(C7), 16455–16464.

Bentamy, A., K. Katsaros, A. Mestas-Nuñez, W. Drennan, E. Forde, and H. Roquet (2003). Satellite Estimates of Wind Speed and Latent Heat Flux over the Global Oceans. *Journal of Climate 16*, 637–656.

Broecker, W., S. Sutherland, and T.-H. Peng (1999). A Possible 20th-Century Slowdown of Southern Ocean Deep Water Formation. *Science 286*, 1132–1135.

Carmack, E. (1974). A quantitative charaterization of water masses in the Weddell Sea during summer. *Deep-Sea Research 21*, 431–443.

Cavalieri, D., C. Parkinson, P. Gloerson, and Z. H.J. (1996, updated 2005). *Sea ice concentrations from Nimbus-7 SMMR and DMSP SSM/I passive microwave data.* Boulder, CO, USA: National Snow and Ice Data Center. June to September 2001, Digital media.

Comiso, J. C., D. J. Cavalieri, C. L. Parkinson, and P. Gloersen (1997). Passive microwave algorithmen for sea ice concentration: A comperison of two techniques. *Remote sensing of enviroment 60*, 357–384.

Doney, S. and M. Hecht (2001). Antarctic Bottom Water formation and deep water chlorofluorocarbon distributions in a Global Ocean Climate Model. *Journal of Physical Oceanography 32*(6), 1642–1666.

Doney, S. and W. Jenkins (1988). The effect of boundary conditions on tracer estimates of thermocline ventilation rates. *Journal of Marine Research 46*, 947–965.

Doney, S., W. Jenkins, and J. Bullister (1997). A comparison of ocean tracer dating techniques on a meridional section in the eastern North Atlantic. *Deep-Sea Research 44*(4), 603–626.

Dutay, J.-C., J. Bullister, S. Doney, J. Orr, R. Najjar, K. Caldeira, J.-M. Campin, H. Drange, M. Follows, Y. Gao, N. Gruber, M. Hecht, A. Ishida, F. Joos, K. Lindsay, G. Madec, E. Maier-Reimer, J. Marschall, R. Matear, P. Monfray, A. Mouchet, G.-K. Plattner, J. Sarmiento, R. Schlitzer, R. Slater, I. Totterdell, M. Weirig, Y. Yamanaka, and A. Yool (2002). Evaluation of ocean model ventilation with CFC-11: comparison of 13 global ocean models. *Ocean Modelling 4*, 89–120.

England, M. H., V. Garcon, and J.-F. Minster (1994). Chlorofluorocarbon uptake in a world ocean model 1. Sensitivity to the surface gas forcing. *Journal of Geophysical Research 99*(C12), 25215–25233.

Fahrbach, E., G. Rohardt, N. Scheele, M. Schröder, V. Strass, and A. Wisotzki (1995). Formation and discharge of deep and bottom water in the northwestern Weddell Sea. *Journal of Marine Research 53*, 515–538.

Fahrbach, E., G. Rohardt, M. Schröder, and V. Strass (1994). Transport and structure of the Weddell Gyre. *Annales Geophysicae 12*, 840–855.

Fichefet, T. and H. Goosse (1999). A numerical investigation of the spring ross sea polyna. *Geophysical Research Letters 26*(8), 1015–1018.

Foldvik, A., T. Gammelsrød, and T. Tørrensen (1985). Hydrographic observations from the Weddell Sea during the Norwegian Antarctic Research Expedition 1976/77. *Polar Research 3*, 177–193.

Foster, T. and E. Carmack (1976). Frontal zone mixing and Antarctic Bottom Water formation in the southern Weddell Sea. *Deep-Sea Research 23*, 301–317.

42

Gammelsrød, T., A. Foldvik, O. Nøst, Ø. Skagseth, L. Anderson, E. Fogelqvist, K. Olsson, T. Tanhua, E. Jones, and S. Østerhus (1994). Distribution of Water Masses on the Continental Shelf in the Southern Weddell Sea. In *The Polar Oceans and Their Role in Shaping the Global Enviroment*, Volume 84, 159–176. American Geophysical Union. Geophysical Monograph 84.

Gloersen, P., W. Campbell, D. Cavalieri, J. Comiso, C. Parkinson, and H. Zwally (1992). Arctic and Antarctic Sea Ice 1978–1987: Satellite Passive-Microwave Observations and Analysis. NASA Special Publication SP-511, NASA, Washington, DC.

Gordon, A. L. and B. A. Huber (1984). Thermohaline stratification below the southern ocean sea ice. *Journal of Geophysical Research 89*(C1), 641–648.

GOSAC (2002). School of Ocean and Earth Science Southampton Oceanography Centre Southampton. http://www.soc.soton.ac.uk/GDD/bio/Yool/GOSAC/gosac_index.html.

Haidvogel, D. B., J. L. Wilkin, and R. Young (1991). A semi-spectral primitive equation ocean circulation model using vertical sigma and orthogonal curvilinear horizontal coordinates. *Journal of Computational Physics 94*(1), 151–185.

Haine, T. and K. Richards (1995). The influence of the seasonal mixed layer on oceanic uptake of CFCs. *Journal of Geophysical Research 100*(C6), 10727–10744.

Haine, T., A. Watson, M. Liddicoat, and R. Dickson (1998, 11). The flow of Antarctic Bottom Water to the southwest Indian Ocean estimated using CFCs. *Journal of Geophysical Research 103*(C12), 27637–27653.

Hall, T., T. Haine, M. Holzer, L. D.A., F. Terenzi, and D. Waugh (2007). Ventilation rates estimated from tracers in the presence of mixing. *Journal of Physical Ozeanography x*(x), 35. accepted.

Hall, T., T. Haine, and D. Waugh (2002). Inferring the concentration of anthropogenic carbon in the ocean from tracers. *Global Biochemical Cycles 16*(4), 78–1–78–15.

Heinze, C., E. Maier-Reimer, and P. Schlosser (1998). Transient tracers in a global OGCM: Source functions and simulated distributions. *Journal of Geophysical Research 103*(C8), 15903–15922.

Hellmer, H. (2004). Impact of Antarctic ice shelf melting on sea ice and deep ocean properties. *Geophysical Research Letters 31*(10), 28–29. L1037 doi:10.1029/2004GL019506.

Hense, I., R. Timmermann, A. Beckmann, and U. Bathmann (2003). Regional and interannual variability of ecosystem dynamics in the Southern Ocean. *Ocean Dynamics 53*, 1–10. doi: 10.1007/s10236-002-0015-6.

Hoppema, M., O. Klatt, W. Roether, E. Fahrbach, K. Bulsiewicz, C. Rodehacke, and G. Rohardt (2001). Prominent renewal of Weddell Sea Deep Water from remote source. *Journal of Marine Research 59*, 257–279.

Huhn, O., H. Hellmer, M. Rhein, W. Roether, C. Rodehacke, M. Schodlok, and P. Schröder (2008). Evidence of deep and bottom water formation in the western Weddell Sea. *Deep-Sea Research II 55*, 1098–1116. doi: 10.1016/j.dsr2.2007.12.015.

Kottmeier, C. and L. Sellmann (1996). Atmospheric and oceanic forcing of Weddell Sea ice motion. *Journal of Geophysical Research 101*(C9), 20809–20824.

Lewis, E. and R. Perkin (1985). The winter oceanography of McMurdo Sound, Antartica. In S. Jacobs (Hrsg.), *Oceanology of the Antarctic Continental Shelf*, Volume 43 of *Antarctic Research Series*, 145–166. American Geophysical Union.

Liss, P. and L. Merlivat (1986). Air-sea gas exchange rates: Introduction and synthesis. In P. Buat-Ménard (Hrsg.), *The Role of air-sea exchange in geochemical cycling*, Volume 185 of *NATO ASI Series. Series C: Mathematical and physical sciences*, 113–127. Dordrecht, Holland: D. Reidel Publishing Company.

Maes, C. and D. Behringer (2000). Using satellite-derived sea level and temperature profiles for determining the salinity variability: A new approach. *Journal of Geophysical Research 105*(C4), 8537–8547. paper number 1999JC900279.

Mensch, M., R. Bayer, J. Bullister, P. Schlosser, and R. Weiss (1996). The Distribution of Tritium and CFCs in the Weddell Sea during the Mid 1980s. *Progess in Oceanography 38*, 377–415.

Mensch, M., W. Smethie Jr, P. Schlosser, R. Weppernig, and R. Bayer (2000). Transient tracer observations during the drift and recovery of Ice Station Weddell. In S. Jacobs and R. Weiss (Eds.), *Ocean, Ice and Atmosphere: Interaction at the Antarctic continental margin*, Volume 75 of *Antarctic Research Series*, 241–256. American Geophysical Union.

Meredith, M., A. Watson, K. van Scoy, and T. Haine (2001). Chlorofluorocarbon-derived formation rates of the deep and bottom waters of the Weddell Sea. *Journal of Geophysical Research 106*(C2), 2899–2919.

Michel, S., C. Tournadre, and N. Reul (2005). Global analysis of sea surface salinity variability from satellite data. *Oceans 2005 - Europe 1*, 11–16. doi: 10.1109/OCEANSE.2005.1511676.

Muench, R., J. Morison, L. Padman, D. Martinson, P. Schlosser, B. Huber, and R. Hohmann (2001, 2). Maud Rise revisited. *Journal of Geophysical Research 106*(C2), 2423–2440.

Nicholls, K. (1997a). New oceanographic data from beneath Ronne Ice Shelf, Antarctica. *Geophysical Research Letters 24*(2), 167–170. Paper number 96GL03922,0094-8534/97/96GL03922$05.00.

Nicholls, K. and K. Makinson (1998). Ocean circulation beneath the Western Ronne Ice Shelf, as derived from in-situ measurements of water currents and properties. In S. Jacobs and R. Weiss (Eds.), *Ocean, Ice and Atmosphere: Interaction at the*

44

Antarctic continental margin, Volume 75 of *Antarctic Research Series*, 301–318. American Geophysical Union.

Nicholls, K., S. Østerhus, K. Makinson, and M. Johnson (2001, 06). Oceanograhic conditions south of Berkner Island, beneath Filchner-Ronne Ice Shelf , Antarctica. *Journal of Geophysical Research 106*(C6), 11481–11492.

Orsi, A., S. Jacobs, A. Gordon, and M. Visbeck (2001). Cooling and ventilating the abyssal ocean. *Geophysical Research Letters 28*(15), 2923–2926.

Orsi, A., G. Johnson, and J. Bullister (1999). Circulation, mixing, and production of Antarctic Bottom Water. *Progress in Oceanography 43*, 55–109.

Orsi, A., W. Nowlin Jr., and T. Whitworth III (1993). On the circulation and stratification of the Weddell Gyre. *Deep-Sea Research 40*(1), 169–203.

Orsi, A., W. Smethie Jr., and J. Bullister (2002). On the total input of Antarctic waters to the deep ocean: A preliminary estimate from chlorofluorocarbon measurements. *Journal of Geophysical Research 107*(C8), 31–1–31–14. doi: 10.1029/2001JC000976.

Pacanowski, R. and S. Philander (1981). Parameterization of vertical mixing in numerical models of tropical oceans. *Journal of Physical Oceanography 11*, 1443–1451.

Rhein, M., J. Fischer, W. Smethie, D. Smythe-Wright, R. Weiss, C. Mertens, D. Min, U. Fleischmann, and A. Putzka (2002). Labrador Sea Water: Pathways, CFC-Inventory, and Formation Rates. *Journal of Physical Oceanography 32*, 648–665.

Rivaro, P., A. Bergamasco, G. Budillon, R. Frache, R. Hohmann, S. Massolo, and G. Spezie (2004). Chlorofluorocarbon distribution in the Ross Sea Water Masses. *Chemistry and Ecology 20*(Supplement 1), S29–S41. (Supplement 1).

Rodehacke, C. B., H. H. Hellmer, A. Beckmann, and W. Roether (2007a). Formation and spreading of Antarctic deep and bottom water inferred from a chlorofluorocarbon (CFC) simulation. *Journal of Geophysical Research 112*(C09001), 1–17. doi:10.1029/2006JC003884.

Rodehacke, C. B., H. H. Hellmer, O. Huhn, and A. Beckmann (2006a). Ocean/ice shelf interaction in the southern Weddell Sea: Results of a regional numerical helium/neon simulation. *Ocean Dynamics 57*(1), 1–11. doi: 10.1007/s10236-006-0073-2.

Roether, W., R. Schlitzer, A. Putzka, P. Beining, K. Bulsiewicz, G. Rohardt, and F. Delahoyde (1993). A chlorofluoromethane and hydrographic section across Drake Passage: Deep water ventilation and meridional property transport. *Journal of Geophysical Research 98*(C8), 14423–14435.

Schlosser, P., J. Bullister, and R. Bayer (1991). Studies of deep water formation and circulation in the Weddell Sea using natural and anthropogenic tracers. *Mar.Chem. 35*, 97–122.

Schröder, M. and E. Fahrbach (1999). On the structure and the transport of the eastern Weddell Gyre. *Deep-Sea Research II 46*(2), 501–527.

Smethie, W. and R. Fine (2001). Rates of North Atlantic Deep Water formation calculated from chloroflurocarbon inventories. *Deep-Sea Research I*(48), 189–215.

Smethie, W., R. Fine, A. Putzka, and E. Jones (2000). Tracing the flow of North Atlantic Deep Water using chloroflurocarbons. *Journal of Geophysical Research 105*(C6), 14297–14323.

Smethie, W. and S. Jacobs (2005). Circulation and melting under the Ross Ice Shelf: estimates from evolving CFC, salinity and temperature fields in the Ross Sea. *Deep-Sea Research I I*(52), 959–978. doi:10.1016/j.dsr.2004.11.016.

Spreen, G., L. Kaleschke, and G. Heygster (2008). Sea ice remote sensing using AMSR-E 89-GHz channels. *Journal of Geophysical Research 113*, C02S03. doi:10.1029/2005JC003384.

Sültenfuß, J. (1998). Das Radionuklid Tritium im Ozean: Meßverfahren und Verteilung von Tritium im Südatlantik und im Weddellmeer. Berichte zur Polarforschung 256, Alfred-Wegener-Institut für Polar- und Meeresforschung, Bremerhaven.

Takahashi, T., S. Sutherland, C. Sweeney, A. Poisson, N. Metzl, B. Tilbrook, N. Bates, R. Wanninkhof, R. Feely, C. Sabine, et al. (2002). Global sea–air CO 2 flux basedon climatological surface ocean pCO 2, andseasonal biological andtemperature effects. *Deep-Sea Research 2*(49), 1601–1622.

Terenzi, F., T. Hall, S. Khatiwala, C. Rodehacke, and D. LeBel (2007). Uptake of natural and anthropogenic Carbon by the Labrador Sea. *Geophysical Research Letters 34*(6), 1–5. doi: 10.1029/2006GL028543.

Thiele, G. and J. Sarmiento (1990). Tracer dating and ocean ventilation. *Journal of Geophysical Research 95*(C6), 9377–9391.

Timmermann, R. (2000). *Wechselwirkung zwischen Eis und Ozean im Weddellmeer*. Dissertation, Universität Bremen, Fachbereich 1, Bremen, Germany.

Timmermann, R. and A. Beckmann (2004). Parameterization of vertical mixing in the Weddell Sea. *Ocean Modelling 6*, 83–100. doi:10.1016/S1463-5003(02)00061-6, CORRECTION in timmermann2005.

Timmermann, R., A. Beckmann, and H. Hellmer (2002). Simulations of ice-ocean dynamics in the Weddell Sea 1. Model configuration and validation. *Journal of Geophysical Research 107*(C3), 10–1–10–9. doi: 10.1029/2000JC000741.

Timmermann, R. and M. Losch (2005). Using the Mellor–Yamada mixing scheme in seasonally ice-covered seas; Corrigendum to: Parameterization of vertical mixing in the Weddell Sea [Ocean Modelling 6 (2004) 83–100]. *Ocean Modelling 10*(3–4), 369–372. doi:10.1016/j.ocemod.2004.11.001.

46

Trumbore, S., S. Jacobs, and W. Smethie Jr (1991). Chlorofluorocarbon evidence for rapid ventilation of the Ross Sea. *Deep-Sea Research 38*(7), 845–870.

von Storch, H. and F. Zwiers (2003). *Statistical analysis in climate research.* Cambridge, UK: Cambridge University Press.

Walker, S., R. Weiss, and P. Salameh (2000). Reconstructed histories of the annual mean atmospheric mole fractions for the halocarbons CFC-11, CFC-12, CFC-113, and carbon tetrachloride. *Journal of Geophysical Research 105*(C6), 14285–14296.

Wallace, D. and J. Lazier (1988). Anthropogenic chlorofluromethanes in newly formed Labrador Sea Water. *Nature 322*(March), 61–63.

Wanninkhof, R. (1992). Relationship between wind speed and gas exchange over the ocean. *Journal of Geophysical Research 97*(C5), 7373–7382.

Warner, M. and R. Weiss (1985). Solubilities of chlorofluorocarbons 11 and 12 in water and seawater. *Deep-Sea Research 32*(12), 1485–1497.

Waugh, D., T. Hall, and T. Haine (2003). Relationships among Tracer Ages. *Journal of Geophysical Research 108*(C5), 7–1–7–16. doi: 10.1029/2002JC001325.

Waugh, D., M. Vollmer, R. Weiss, T. Haine, and T. Hall (2002). Transit time distributions in Lake Issyk-Kul. *Geophysical Research Letters 29*(24), 84–1–84–4. doi: 10.1029/2002GL016201.

Weiss, R., J. Bullister, R. Gammon, and M. Warner (1985). Atmospheric chlorofluoromethanes in the deep equatorial Atlantic. *Nature 314*, 608–610. doi: 10.1038/314608a0.

Weppernig, R., P. Schlosser, S. Khatiwala, and R. Fairbanks (1996). Isotope data from Ice Station Weddell: Implications for deep water formation in the Weddell Sea. *Journal of Geophysical Research 101*(C10), 25723–25739.

Wu, J. (1996). Air-sea gas transfer: Meachanisms and parameterization. *Journal of Physical Oceanography 26*, 1440–1447.

Zheng, M., W. De Bruyn, and E. Saltzman (1998). Measurements of the diffusion coefficients of CFC-11 and CFC-12 in pure water and seawater. *Journal of Geophysical Research 103*(C1), 1375–1379.

47